INFORMATION TO USERS

This manuscript has been reproduced from the microfilm master. UMI films the text directly from the original or copy submitted. Thus, some thesis and dissertation copies are in typewriter face, while others may be from any type of computer printer.

The quality of this reproduction is dependent upon the quality of the copy submitted. Broken or indistinct print, colored or poor quality illustrations and photographs, print bleedthrough, substandard margins, and improper alignment can adversely affect reproduction.

In the unlikely event that the author did not send UMI a complete manuscript and there are missing pages, these will be noted. Also, if unauthorized copyright material had to be removed, a note will indicate the deletion.

Oversize materials (e.g., maps, drawings, charts) are reproduced by sectioning the original, beginning at the upper left-hand corner and continuing from left to right in equal sections with small overlaps.

Photographs included in the original manuscript have been reproduced xerographically in this copy. Higher quality 6" x 9" black and white photographic prints are available for any photographs or illustrations appearing in this copy for an additional charge. Contact UMI directly to order.

ProQuest Information and Learning
300 North Zeeb Road, Ann Arbor, MI 48106-1346 USA
800-521-0600

Energy Transfer and Waveguide Studies of Eu^{3+} and Tb^{3+} Doped 2 SiO_2-TiO_2 Glass Prepared via the Sol-Gel Route

Carmela Mancuso

A Thesis

in

The Department

of

Chemistry and Biochemistry

Presented in Partial Fulfillment of the Requirements
for the Degree of Master's of Science at
Concordia University
Montreal, Quebec, Canada

December 2001

ABSTRACT

Energy Transfer and Waveguide Studies of Eu^{3+} and Tb^{3+} Doped 2 SiO_2-TiO_2 Glass Prepared via the Sol-Gel Route

Carmela Mancuso

In recent years, waveguide studies have played an active role in the telecommunication industry. High doping concentrations, is essential in the manufacture of short and compact optical amplifiers yet quenching can reduce the performance of the amplifier. Sol-gel chemistry, combined with the dip-coating method is a means to develop rare-earth doped planar waveguides for such integrated optics components.

The sol-gel process involves three main steps: first, a metal alkoxide (Si-alkoxide) in alcohol-based medium undergoes hydrolysis at a predetermined pH; the next step involves condensation, where Si-OH tetrahedra linkages occur and eventually result in an SiO_2 network. The third step involves solvent evaporation to eliminate residual organics and hydroxyl groups within the pores of the gel.

This thesis reports on the luminescence properties of Eu^{3+} and Tb^{3+} within the SiO_2-TiO_2 host prepared via the sol-gel method with both H_2O and D_2O hydrolyzed systems. Eu^{3+} and Tb^{3+} have long been used as phosphors and laser materials because of their sharp and intense emissions due to f-f electronic transitions. Lifetime studies and emission spectra have determined that D_2O decreases the non-radiative decay rate. The smaller non-radiative decay rate causes enhancement of fluorescent intensity and increases the measured transition lifetime. We also examined the potential energy

transfer mechanism between Tb^{3+} and Eu^{3+} co-doped at 3 mol % in the glass host. It was observed that at this concentration, energy transfer occurs from the Tb^{3+} donor ion to the Eu^{3+} acceptor ion. This non-resonant energy transfer process covers a gap of ~3500 cm^{-1}. Raman studies show that the cut off phonon energy is ~1100 cm^{-1} suggesting that this energy transfer is approximately a three phonon process.

Sol-gel synthesis and dip-coating methods were used to develop a planar waveguide for a 5 mol % europium sample in the aforementioned host. Emission studies show. that the spectrum has a stronger luminescent intensity, and. it was observed that presence of hydroxyl groups is greatly reduced as compared to the conventional glass at the same concentration.

ACKOWLEDGMENTS

This thesis would not have been possible without the help of Dr. J.A Capobianco and my committee members, Dr. R. Le Van Mao and Dr. C. Skinner.

Thank you to Dr. M. Bettinelli (University of Verona, Italy), for all his insight and advice throughout this project.

A special thank you goes out to my family especially to my mother and sister who supported me, loved me, and pushed me to do the best I can. Thank you Kathy and Denis Gauvin for your advice and support, it meant a lot.

Thank you Shawn for being my soul mate, for your patience and understanding and for making me realize that I can do anything I put my mind to.

Last but not least, I would like to thank my very best friend Tania D'Alesio for all her support, love and patience during these last few years. Thank you Elham for all your help and for sharing your wisdom.

TABLE OF CONTENTS

CHAPTER 5

LIST OF FIGURES

LIST OF TABLES

CHAPTER 1

1.0 INTRODUCTION

1.1 Sol-Gels

Sol-gel derived systems are a subject of considerable interest, due to the study of their amorphous structure and how their structure compares to that of their glass melt counterparts. Preparation of these inorganic materials via chemical routes has shown to be an important field of research in the synthesis of ceramic powders, fibers, and through waveguide technology. lasers with a wide range of tunability can be constructed. Interest in the sol-gel process began as early as the mid-1800's with work by Ebelman [1] and Graham [2]. They observed. that upon hydrolysis of a metal alkoxide of tetraethylorthosilicate. under acidic conditions, yielded SiO_2 in the form of a "glass-like material". Ebelman and Graham ran into problems when it took them one year or more of drying in order to avoid the silica gels from turning into powder. Between the 1800's to 1920's. chemists became interested in gels due to the phenomenon of the Liesegang Rings formed from gels. Many well-known chemists such as Ostwald [3] and Lord Rayleigh [4] investigated the problem of the periodic precipitation phenomena that leads to the formation of the Liesegang rings and the growth of crystals from gels [5]. Over the years, this process was further refined and in the 1950's and 60's Roy and coworkers [6] used the sol-gel process to produce a large number of ceramic oxide compositions that included such metals as Al, Si, Ti, and Zr etc. During the same period of time, Iler's [7] work lead to the commercial development of colloidal silica powders namely DuPont's colloidal Ludox spheres. Work done by Stober et al. [8] which was an extension of Iler's findings showed that base catalysis of tetraethylorthosilicate undergoing hydrolysis by water could

control both the morphology and particle size of powders giving rise to Stober spherical silica powder. The Stober process therefore became known as the controlled growth of monodisperse silica microspheres. Schroeder [9] in 1969 produced oxide layers deposited from organic solutions and he further described processes such as dip-coating, spinning and spray coatings which are all methods that are presently used in the production of planar waveguides. He further introduced the concept of having single as well as multi-component oxides, which play a major role in the research of sol-gel technology.

The incorporation of rare earth ions within sol-gels has lead to important research in the area of telecommunications due to the fact that sol-gels containing high concentrations of rare earth ions can be used to manufacture compact planar waveguides. This research can then branch off into the production of optical amplifiers used in fiber optic cables, as well as in the synthesis of coatings on optical memory discs and superconductors.

A sol is defined as a colloidal dispersion of particles in a liquid. A gel is a substance that contains a continuous solid skeleton enclosing a continuous liquid phase; the liquid prevents the solid from collapsing; and the solid prevents the liquid from escaping [10]. The sol-gel process therefore enables materials to be brought out of solution either as a colloidal gel or a polymerized macromolecular network whilst still remaining a solvent [11].

Colloids exist in many forms and have technological importance. They can be found in several materials, which we use in our daily life such as in, cosmetics, aerosols, paints, and in our foods in the form of food thickening agents.

The most preferred starting materials in the production of these colloids include metal alkoxides, which have the following general formula:

$$\mathbf{M\,(OR)_n}$$

Where M = metal

R= alkyl group

n = valence number of the atom

The metal alkoxides pertinent to this research are TEOS (tetraethylorthosilicate) and Ti(IV) Isopropoxide.

There are many advantages in utilizing the sol-gel method, as opposed to conventional glass melt methods. Primarily, this process provides good homogeneity and uniformity within the sample whether it is a sol-gel or a waveguide. Secondly, there is an ease of composition and control at the molecular level, which enables these materials to be shaped at room temperature. The above statements enable flexibility in producing bulk gels with specific dimensions, spin fibers and produce waveguides through the dip-coating method. Lastly, the low processing temperature is ideal since all samples are prepared at room temperature and in this thesis, samples are annealed at temperatures not more than $200^{o}C$. The glass industry can therefore benefit from sol-gel technology for two main reasons. Primarily, it is possible to produce high-priced existing products, such as titanium silicate ULE glasses or graded-index optical fibers, more cheaply and with a higher quality. Usually, only expensive glass products are targeted since the high cost of raw materials (silicon or metal alkoxides are employed rather than silicon or metal oxides) make large quantity production commercially nonviable. The sol-gel process should not be seen as a complete substitute for the raw materials usually employed in industry but rather when

high-priced articles are concerned [12]. Lastly, considerable energy savings can be achieved since the porous structure of the gel does not need to attain high liquid melt temperatures to form the glass.

Once the gel is produced, the process of drying is required in order to achieve the final densified sol-gel. Delicate drying and sintering is needed in order to obtain the desired material that has as little water as possible in order to prevent signal quenching due to hydroxyl groups and to ensure that we have a stabilized gel that is free from stresses that could be caused by re-hydration. The rate of drying and temperature range are important depending on what type of materials are to be produced, e.g. ceramic powders, monolithic shapes (which usually require a week to dry), xerogels (usually require one month of drying), and aerogels which require careful extraction of solvent. Many difficulties are encountered upon drying due to the fact that at various temperature ranges the gels undergo shrinkage mainly to capillary forces, which can cause the sample to crack and break.

The sol-gel process can be summarized in Figure 1.1.1.[13]

1.2 Waveguides

At the end of the 18th century, the optical telegraph, which was developed by Claude Chappe, [14] allowed the transmission of a signal over the 423 km distance from Paris to Strasbourg within a time of six minutes [15]. The replacement of the optical telegraph by the electrical telegraph in the middle of the 19th century allowed for a faster signal transmission. Graham Bell [16] in 1880 reported on the transmission of speech over a light beam in which he used a diaphragm-mirror against the back of which the

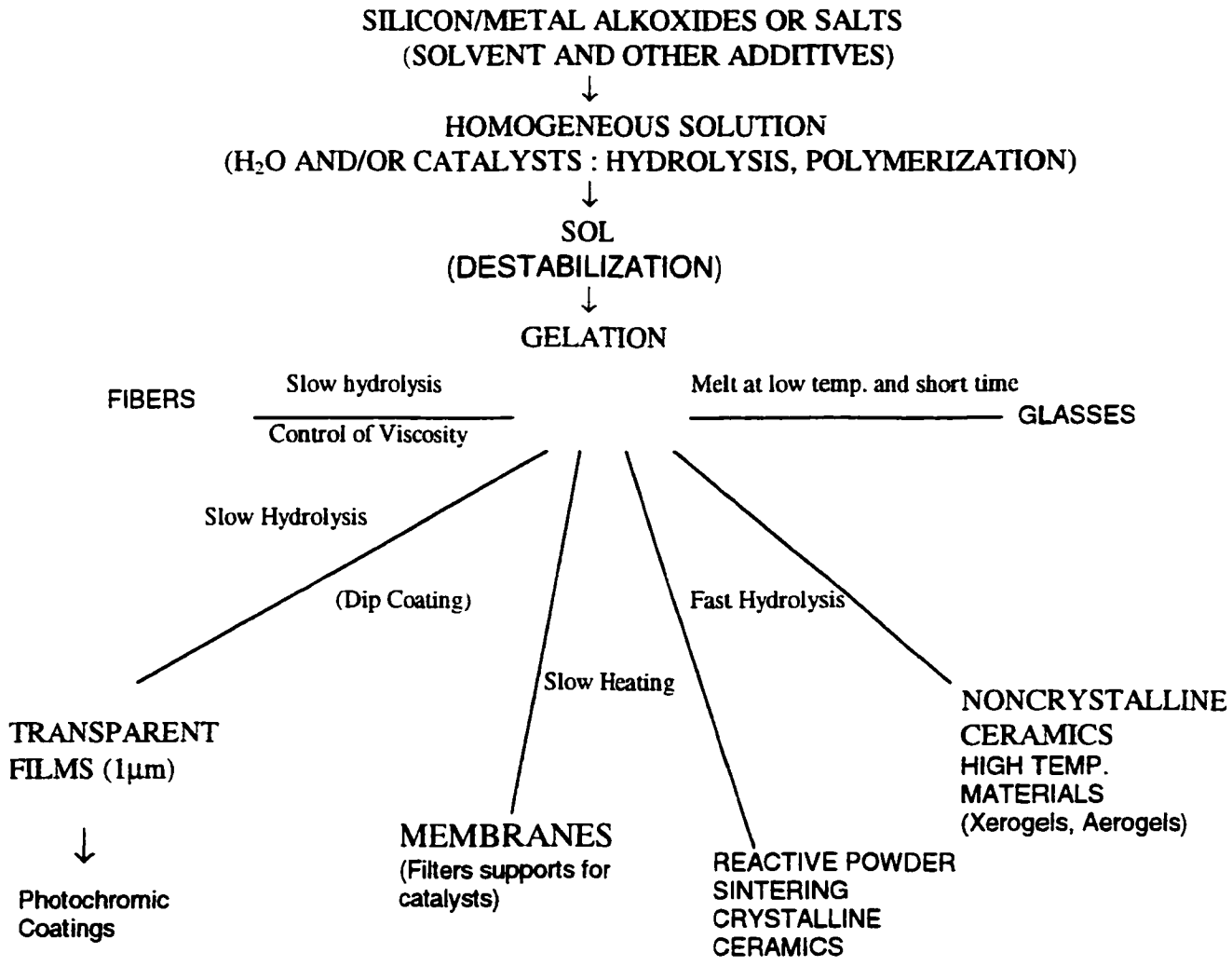

Figure 1.1.1: Starting materials and end products as a result of the sol-gel process.

speakers voice was directed. A parabolic reflector was used to receive the beam and was consequently focused on a sensitive selenium photo-resistor, which was connected to a battery and a telephone. Bell had proposed modulators based upon the Faraday effect and Kerr effect. In the first half of the twentieth century, optical communications were used only on a small-scale in mobile low-bandwidth and short distance communication links, this all changed at a very fast pace through the invention of the laser. Research in optical communication was greatly stimulated by the use of coherent light due to the following reasons: The carrier frequencies between 10^{13} and 10^{15} Hz yield a high available bandwidth for signal transmission. Another important reason is that the spatial coherence of the laser light yields a lower beam divergence. This is advantageous not only for free-space communications but also the coupling efficiency into optical beam waveguides [15]. The objectives in obtaining optical waveguides is to develop a family of optical and electro-optical elements in a thin-film planar form that will allow the integration of a large number of devices on a single substrate [15]. Anderson [17] in 1965 proposed the basic ideas behind these integrated optical components. He suggested that since the microfabrication technology lead to the development of electronic circuit structures on a scale of micrometers, it was then possible to use this type of technology to develop monomode optical devices in semiconductor or dielectric materials. Optical waveguides have also been fabricated in order to avoid disturbances by the atmosphere. Whereas light waves in free space propagate in a straight line, waveguides in all practical cases are forced to follow a curved path as determined by the terrain contours and diverse physical obstacles [18]. The two major considerations in addressing the transmission of light-wave energy through an optical fiber are transmission loss and signal distortion. If the signal

being transported is analog in nature, then the distortion will be quite similar to that incurred in other analog transmission bandwidth and noise. If the signal being transported is digital, the interference will be evidenced as pulse distortion or dispersion, i.e. pulse broadening. Almost all the experiments in the past were performed invariably in bulk materials and with a light beam of nearly Gaussian intensity distribution. Waveguides are produced using three different types of coating techniques such as dip coating, spin coating and spray coating. Dip-coating is most relevant in this thesis and is one of the most common methods used. This method is quite simple and consists of dipping a substrate in a solution, withdrawing at constant speed and firing at various temperatures. The advantages of using the sol-gel and dip-coating techniques for depositing thin films are well known and include the ability to coat complex shapes and large surfaces. The use of non-sophisticated low cost equipment is also a great advantage. The disadvantages in the utilization of this type of method include the long processing time and the shrinkage and non-uniformity of the coatings. Recently, however, the introduction of prism-films and grating couplers, have raised important questions concerning the future needs of optical systems [19]. Prism-films have lead to a more sophisticated approach in the telecommunications industry through the use of waveguides. At high doping concentrations, optical amplifiers have the ability to amplify light signals for several hundred kilometers.

A waveguide traps and guides a light-beam incident at a certain angle, in a zig-zag fashion along a certain propagation distance, between two loss-less, dielectric media. This type of medium is needed in the production of waveguides that have minimal losses in intensity with maximum signal. These films are then used in the telecommunication

industry through the use of optical amplifiers. The advantage of these thin films is that the elements of a thin-film device are exposed on the surface and are easily accessible for probing, measurement, or modification. Secondly, compared to microwaves, the optical wavelength is a factor of 10^4 smaller [19]. The thin-film can be made small and thus placed one next to the other on a single substrate forming a compact optical system that is less vulnerable to environmental changes and hence more economical. Since film thickness is comparable to the optical wavelength, and since most of the light is confined within the guide, the light intensity inside the guide is large even at moderate laser power. A well-known optical waveguide is the optical fiber, which has a characteristic circular cross section. In contrast, the guides of interest to integrated optics are usually planar structures such as planar films or strips [20].

The cross-section of a planar waveguide is shown as follows:

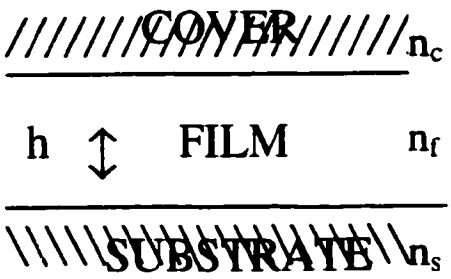

This cross-section consists of a thin film of thickness h and refractive index of n_c, n_f, and n_s, which refer to the index of refraction of the cover, film and substrate respectively. The index of refraction of the cover is usually 1.0 since it corresponds to the index of air. It could also be at 1.46, which is the index of refraction of a soda-lime microscope slide and is what is commonly used as the substrate. Substrates are needed due to the fact that thin films are usually on the order of 1 μm or less and thus need to be

supported [20]. In order to confine and support propagating modes within the thin-film, the index of refraction of the film must be greater than that of the substrate and cover. The index of refraction of the substrate can be greater or equal to that of the cover.

The development of light-wave couplers is a step forward in the ongoing research in the field of telecommunication and film optoelectronics. By coupling a laser beam efficiently in and out of any thin-film structure, any single mode of light-wave propagation can be achieved. In both the prism-film and grating couplers, a light beam is fed into a film through a broad surface of the film and thus avoids the difficult problem of focusing a light beam through a rough film edge. Since the film and the prism are coupled over a length of many optical wavelengths, energy transfer can be imagined to occur and take place continuously between them as waves propagate over the coupled region [19].

1.3 Laser Spectroscopy and Characteristics of Europium and Terbium

According to quantum theory, molecules possess sets of discrete energy levels, and the energy, which any individual molecule can posses is limited to one of these values. The majority of molecules, at any moment in time, exists in the state of lowest energy called the ground state, and is often by the absorption of light that transitions to states of higher energy can take place. Since only discrete energy levels exist, there results, a certain selectivity over the frequencies of light that can be absorbed by any particular compound; this principle underlying most of spectroscopy [21]. Laser spectroscopy therefore, can be used in order to study the energy levels associated to transition and rare earth ions. Depending on the wavelength and sample, the laser light excites the molecules in the

ground state to a higher excited state. Emission from the higher excited state to the lower states can then be observed.

Gadolin, a Finnish chemist in 1794 isolated *yttria* from a mineral that had been discovered at Ytterby, a village near Stockholm in Sweden [22]. He believed that yttria was an oxide of a single new element but further research confirmed it to contain other oxides no fewer that ten new elements including: yttrium, terbium, erbium, ytterbium, scandium, holmium, thulium, gadolinium, dysprosium, and lutetium [22]. Klaproth, Berzelius and Hisinger, soon after isolated an oxide, known as *ceria*, which later was shown to contain, cerium, lanthanum, praseodymium, samarium, and europium. Europium and terbium both belong to the rare earth series, which contains 14 elements with atomic numbers between 57 and 71. The rare earth metals contain 4f electrons and are electropositive with a common valence state of 3+. Europium and terbium are the rare earth ions of study in this thesis and have the following configurations:

$$Eu^{3+}\ [Xe]\ 4f^{6}$$

$$Tb^{3+}\ [Xe]\ 4f^{8}$$

Their respective energy level diagrams can be seen in Figure.1.3.1. The lanthanide and actinide metals are unique in that their atomic radii decrease as the atomic number increases thus the trend is called lanthanide or actinide contraction. Although there is a gradual reduction in radius from Ce^{3+} to Lu^{3+}, there are breaks in the trend namely at europium and ytterbium. The contraction arises from the poor ability of f electrons to screen the other valence electrons from the nuclear charge. All of the rare earth metals except europium and ytterbium may be considered to consist of Ln^{3+} ions with three

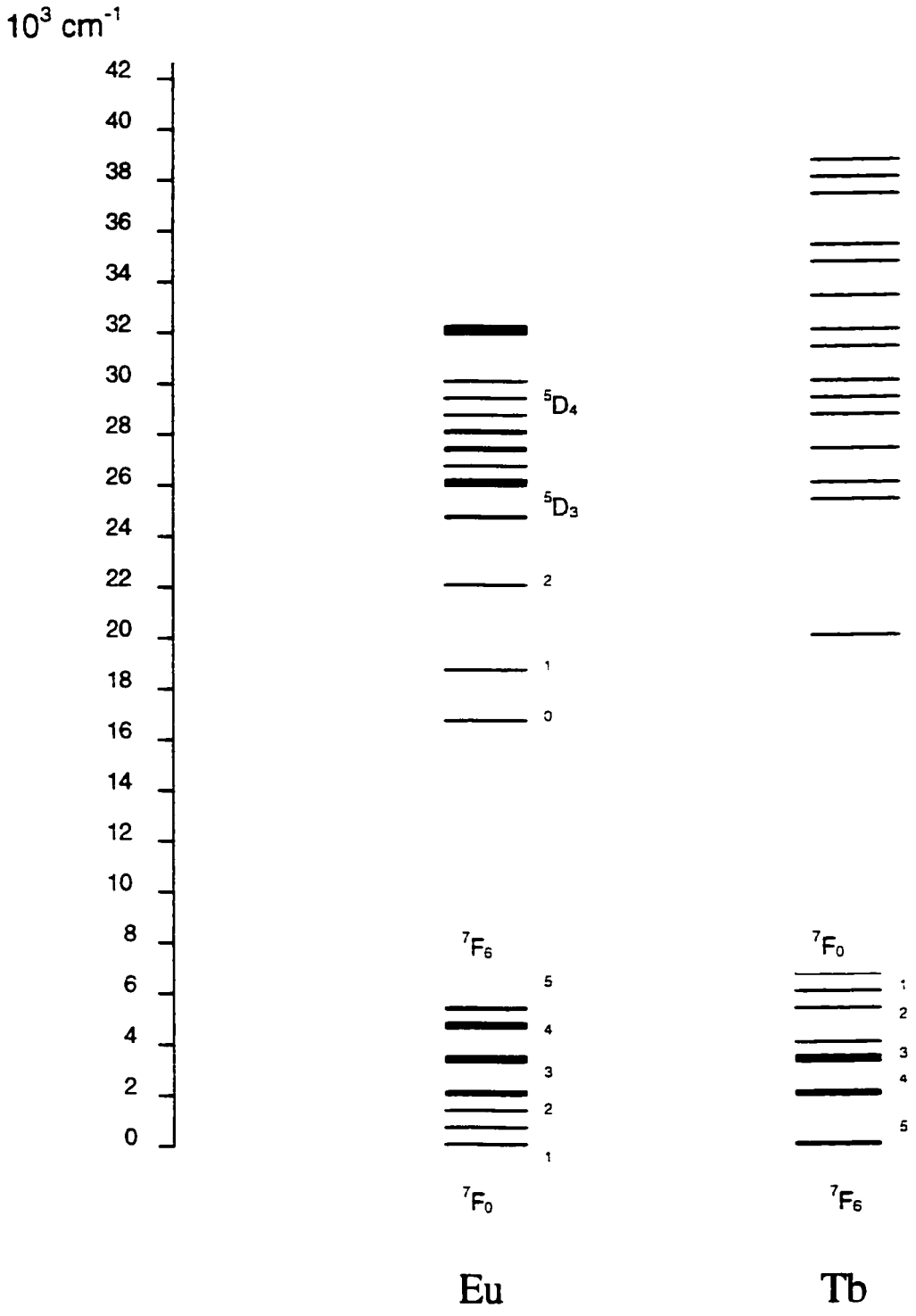

Figure 1.3.1: Schematic representation of the energy levels for Eu and Tb.

electrons per atom devoted to metallic bonding. This accounts for the greater metallic radii of Eu and Yb, with respect to the other rare earth ions [22]. Since Eu^{3+} and Tb^{3+} posses good luminescence characteristics based on the 4f electronic transitions, they have been studied for practical applications as phosphors [23]. Europium and terbium ions have been studied extensively due to their potential for energy transfer and their enhanced optical properties.

1.4 Energy Transfer

Energy Transfer processes are extremely important in solid state laser systems because they provide an enhancement of luminescence emission as well as consequent reduction of the laser threshold [24]. The general purpose of studying these types of processes is to investigate the possibility of increasing the efficiency of the phosphor or laser. The concept of energy transfer, was first introduced by Forster [25] in 1948. Energy transfer was studied in organic molecules with electric dipole-dipole interactions for allowed transitions only. Later, Dexter [26] modified energy transfer interactions to include forbidden transitions allowing for the study of energy transfer between rare earth ions and inorganic solids. Inokuti and Hirayama [27] later developed the theory for the exchange coupling. To account for the concentration quenching of the luminescence, Botden [28] proposed the theory of relaxation by migration, which was further developed by Dexter and Schulman [29]. Phonon-assisted energy transfer plays a major role in the infrared to visible conversion process in some phosphors, which are activated with trivalent rare earth ions as demonstrated by Hewes et al [30], and Johnson et al [31]. The terminology of phonon-assisted energy transfer refers to a nonresonant energy transfer process where the

mismatch of energy between the donor and acceptor ions is compensated through simultaneous emission or absorption of one or more phonons depending on the cutoff phonon energy. The cutoff phonon energy refers to the highest lattice vibration within the host sample (SiO_2-TiO_2) observed through Raman scattering techniques.

Energy transfer mechanisms in sol-gels have been studied for various rare earth ions. Wang et al [32] studied the energy transfer processes between β-diketonate ($ttfa^-$) ligands and europium (III) using time-resolved luminescence spectroscopy. Other studies include work by Murakami et al [33] and their work on the energy transfer processes of Eu^{3+}, Nd^{3+} and Cr-doped sol-gel PLZT (lead zirconate titanate) ceramics. To the best of our knowledge, the only energy transfer studies using the SiO_2- TiO_2 host were performed by Fu et al [34] on the energy transfer between UO_2^{2+} and Eu^{3+} in a sol-gel derived titania matrix. Titanium dioxide as a host has been studied extensively and is widely used for the manufacture of waveguides due to its wide range of refractive index. Energy transfer between Eu^{3+} and Tb^{3+} has been studied in various hosts including Y_2O_3 [35] and cubic hexachloroelpasolite [36] and has not been reported in a silicon-titanium host and thus one of the objectives in this thesis.

1.5 Statement of Purpose

Optical device materials prepared via the sol-gel method are of current technological interest. In particular, sol-gels derived from silica glass doped with rare earth ions are an important class of sol-gel optics, which include solid-state lasers and fiber amplifiers [37]. The sol-gel technique has been used extensively to make improved glasses and ceramic materials at low cost in the production of thin films, coatings, fibers, composites and

improved bulk materials. The synthesis of sol-gels provides ease of composition and microstructural control at the molecular level with the ability to shape the sol-gel at room temperature.

The spectroscopic properties of Eu^{3+} and Tb^{3+} in an SiO_2-TiO_2 host was the primary interest for this thesis, due to the fact that to the best of our knowledge, these studies have not yet been done. Energy transfer between rare earth ions has also been studied in sol-gel systems as in glasses and crystals. The energy transfer between Tb^{3+} and Eu^{3+} has been investigated in a variety of hosts such as in Y_2O_3 [35] and in cubic hexachloroelpasolite [36] yet no energy transfer studies of these two rare earth ions in a silica-titania host have been investigated and thus a further interest to this thesis.

Waveguide studies using silica-titania hosts are of technological importance due to their large range of index of refraction. The index of refraction ranges anywhere between 1.46 (glass slide) to 2.2 (amorphous TiO_2) depending on the amount of titanium in the system. Rare earth doped planar waveguides at high concentrations, are at the present an active field of work in the research of optical amplifiers and new laser sources for integrated optic devices. Waveguides with a silica-titania host have been investigated for Er^{3+} [38] yet waveguides doped with high concentrations of Eu^{3+} have not been presented in literature and thus these results will be presented in this thesis.

Although many studies have been performed on sol-gel systems, little is known about the structure of the sol-gel and about the coordination of the rare earth ions. Computational techniques have been an important tool in providing information about the order of sol-gels systems and local structure. In this thesis, the objective is to use Raman

scattering and infrared techniques to understand the types of stretches and coordination involved within the disordered sol-gel system.

CHAPTER 2

2.0 THEORY

2.1 Chemistry of Sols

In this section, the physical chemistry behind the synthesis of these sols and what types of interactions take place from homogeneous liquid to viscous gel will be presented.

Molecules and atoms can sometimes form conglomerates under the influence of intermolecular forces. If these conglomerates remain stable then they are referred to as colloids. These colloidal particles are usually 500 nm or less in size and cannot be seen using a normal optical microscope since their maximum size is $\leq$ to the wavelength of light. Light scattering techniques are usually used in order to obtain information about the size, shape, and the intercation between such particles. One of the interests in this thesis is the study of sols, which are the colloidal suspension of a solid in a liquid.

The thermodynamics of these macromolecules dissolving in solution, tells us that the entropy change is important and should be taken into consideration. The process of macromolecules dissolving in solution is non-ideal since these molecules displace large amounts of solvent instead of simply dissolving. There is a large excluded volume, which means that a molecule is unable to "swim" freely through the solution because it is not able to occupy regions where there are similar molecules [11].

If there is an interaction between the solvent molecules and functional groups that can be found on the macromolecule then the enthalpy of solution should also be taken into consideration. The process described above can be considered as a dynamic process in equilibrium. If the density of the solid is higher than that of the liquid, the solid will tend to precipitate out of solution. According to thermodynamics, any particle with a high

specific surface area will have an associated high surface energy. The work needed to increase the surface area of a particle by a small increment, $d\sigma$, is equal to the product between the force that resists the increase in area and the distance it moves.

The surface tension experienced by most materials can be represented as X, and the increment of work represented as dw is given as follows:

$$dw = Xd\sigma$$

Using the above equation and taking into consideration the Helmholtz function(dA) that relates the change of state of a system to entropy (S), p-v work and surface creation, the following equation is obtained:

$$dA = -S\,dt - pdV + Xd\sigma \qquad (2.1.1)$$

dA Helmholtz function
S entropy
T temperature
p/V pressure/volume

All systems favor a low Helmholtz energy dA thus the system attempts to lower its internal energy and increase entropy and disorder. The Helmholtz function takes into consideration the changes in a system occurring at constant temperature and volume as opposed to the Gibb's free energy, which takes into consideration changes at constant pressure and not at constant volume. From this it should be apparent that thermodynamically the colloidal state should not exist yet experience tells us that it is common. The stability of a colloid is therefore a kinetic one where the particles in the solvent are trying to collapse, to move towards one another and coalesce to reduce surface area [11].

2.2 The Formation of Gels

As sol particles grow and collide the clusters tend to overlap and become nearly immobile. Condensation then occurs where bonds form and a network is developed and thus macroparticles are formed. The sol will therefore become a gel when it can support a stress elastically. The activation energy cannot be measured, nor can one precisely define the point where the sol changes from a fluid liquid into a viscous gel. The change is gradual as more cross-linking develops [5]. A solvent in an inorganic system usually has a density between 1 g/cm^3 and 1.5 g/cm^3 and solids can range anywhere between 2.2 and 3.8 g/cm^3. If aggregation is allowed to take place, the solid particles will want to settle out of the solution. Depending on the initial starting materials and structure of the sample, the solid will occupy a certain volume in solution. This final volume depends greatly upon the state of aggregation of the colloidal particles in solution.

Three different processes may occur that demonstrate the types of aggregation involved. These processes, have been described by Jones [11] as follows:

1. Large, peptized particles pack densely to form sediments, which will not re-disperse.
2. Particles, which are partially aggregated, have bridging capability and therefore give loose sediments, which can often be re-dispersed.
3. In many cases the volume of this sediment may well equal the volume of the complete solution.

In the third case, the macromolecules or particles have aggregated in such a way as to form a continuous three-dimensional network throughout the whole volume of the original solution.

The first process is categorized as a peptized colloid in which the sedimentation volume is about one third of the original volume. Peptization is a method of achieving good dispersion in solution by controlling the composition of the dispersed solution. The second process shows aggregated particles in which the volume of sedimentation is about half that of the original volume. Aggregate particles can bond together to form a solid mass. The last process is considered a gel in which the sedimentation volume is equal to that of the original volume giving as well dispersed particles distributed and suspended within the liquid. In this case cross-linking has occurred giving the desired network, which exhibits the visco-elastic properties of a gelatinous mass. This state is called a gel. The overall state of a gel is determined by the number of cross-links as well as the type of catalyst used, i.e. an acid or base.

2.3 Formation of Sols

There are basically two routes to the formation of colloidal sols. One consists of breaking down a material from a macroscopic to a microscopic state and this can be achieved through different methods such as milling or grinding, discharge between electrodes, and electrolytic deposition [11]. In this thesis the major interest is in the chemical route in obtaining sols. These routes involve the development of an insoluble species by a chemical reaction in solution. It is important to note that the final form of this sol is dependant on the concentration of the reactants, and the preparation conditions (i.e. pH, temperature). The fact that many factors may be varied in the preparation of these sols give scientists the flexibility and control to synthesize a large number of different sols using different types of starting materials.

There are also different types of techniques that can be utilized to obtain sols such as precipitation techniques, solvent extraction, and hydrolysis methods.

Different types of techniques lead to different types of sol-gels. The generation of an hydroxide or hydrated oxide by hydrolysis is usually considered a precipitation reaction since quite often the hydrous oxide precipitates out of solution in the form of a gel. This gel can further be processed to coagulate the particles from the gel to form a precipitate. By forming colloids and precipitates the particle distribution within the solution is narrower. An example of this method involves the use of silica. Silica can be formed through the addition of sulfuric acid to sodium silicate. The acid removes the water in the system leaving behind either precipitated silica's or further processed to achieve monolithic silica pieces.

Another technique in the preparation of sols is through solvent extraction. This type of technique is usually what is used to prepare aerogels, which have homogeneously dispersed air pockets within the gel. Jones [11] gives an example of a titanium dioxide sol, which is prepared starting from a concentrated aqueous acidic solution of titanium chloride. This solution is clearly an ionic one. He states that the precipitation of crystalline titania in solution is found to occur at a particular Cl :Ti ratio of approximately 1:5. It is therefore necessary to remove the hydrolytic acid from the solution, which can be achieved using an immiscible organic amine. This amine will then combine with the anions of the acid and form nitrates or chlorides depending on the acid present.

The hydrolysis method, which is the last technique presented in this section touches upon the use of alkoxides in the preparation of true colloidal sols. It is known in the sol-gel technique that upon hydrolysis of an alkoxide solution at a pH less than 7 under controlled

conditions will yield a complex structure of inter-linking polymeric strands. Silica sols that are prepared upon hydrolysis of tetraethylorthosilicate give rise to monodispersed spheres. Stoeber [8], as mentioned in the introduction discovered that there is a direct relationship between the size of particles and the amounts of water and base added to the solution. He also observed that the alkyl group determines the rate of reaction where methyl was the fastest and tetrapentyl the slowest.

2.4 Sol-gel Process

In the previous section, the definition of colloidal particles and the physical aspects of this sol-gel chemistry has been discussed. In this section, the various steps in the production of sols is outlined in detail. In the introduction, the definition of a metal alkoxide was given, and the alkoxides pertinent to this thesis were discussed. As previously mentioned, the starting solution consists of a metal alkoxide in an organic solvent that undergoes hydrolysis and condensation. It must also undergo catalysis under acidic or basic conditions. The final stage involving evaporation, and the rate of drying, are essential to achieving a sol-gel that is stable, homogeneous, free from hydroxyl groups, and crack free.

2.4.1 Hydrolysis and Condensation

The transition from sol to gel is a very delicate one in which the starting reactants and conditions will predict the shape, composition, and concentration of the final product. The two main steps that the sol must undergo initially are hydrolysis and condensation.

In the hydrolysis process, the alkoxide groups (OR) of the metal alkoxide are replaced by hydroxyl groups (OH) as shown in equation 2.4.1.1 and 2.4.1.2.

$$M\text{-}OR + H_2O \rightarrow M\text{-}OH + ROH \quad (2.4.1.1)$$

$$Si(OC_2H_5)_4 + H_2O \rightarrow Si(OH)(OC_2H_5)_3 + C_2H_5OH \quad (2.4.1.2)$$

There are many different types of silicon alkoxides including tetramethylorthosilicate abbreviated TMOS and tetraethyorthosilicate abbreviated TEOS. TEOS is also referred to as tetraethyoxysilane and ethyl silicic acid [39]. Whichever name is used this alkoxide is a common precursor in the sol-gel process.

The byproducts of the hydrolysis reaction are alcohol groups. As shown in reaction (2.4.1.2) TEOS undergoes hydrolysis at a 1:1 ratio with water, the hydroxide group successfully replaces an alkoxide group and produces a byproduct of ethanol. Following hydrolysis there is the subsequent condensation reaction, which involves the silanol groups. These silanol groups come together to form siloxane bonds and the water and alcohol released from the reaction remains in the pores of the network. Equations 2.4.1.3 and 2.4.1.4 show the reactions.

$$MOR + HOM \rightarrow MOM + ROH \quad (2.4.1.3)$$

$$Si(OC_2H_5)_4 + \equiv Si(OH) \rightarrow \equiv Si\text{-}O\text{-}Si\equiv + C_2H_5OH$$

$$MOH + HOM \rightarrow MOM + H_2O \quad (2.4.1.4)$$

$$\equiv Si(OH) + OH\text{-}Si\equiv \rightarrow \equiv Si\text{-}O\text{-}Si\equiv + H_2O$$

Equations 2.4.1.3 and 2.4.1.4 involve the use of TEOS. Silicon hydroxide groups react with the metal alkoxide to form these metal-oxygen-metal bonds. These metal-oxygen-metal groups will bond together in order to form a 3 dimensional network. When sufficient interconnected Si-O-Si bonds are formed in a region, they respond cooperatively as colloidal particles or a sol.

2.4.2 Acid and Base Catalysts

There are two different types of catalyst that can be utilized in the sol solution either an acid or base. An acid catalyzed reaction usually refers to a solution that has a pH range from approximately 1 to 2.5. A basic catalyzed solution has a pH range from approximately 2.5 to 3.5 [40]. The pH range for the base catalyzed reaction is based on the general mechanism and not on the pH. The hydrolysis reaction appears to be specific acid or base catalyzed. Acid catalysts protonate the alkoxide group which makes a better leaving group of ROH. Base catalysts reactions dissociate water producing a strong nucleophile of OH^-. The condensation reaction depends on the acidity of the silicate reactants. Above about pH 2, acidic silanols are deprotonated; and $\equiv Si\text{-}O^-$ are created. Weakly acidic silanols or ethoxides are protonated at a pH below 2 producing good leaving groups such as H_2O and ROH. Through the formation of these leaving groups, the requirement of charge transfer in the transition state is avoided. The esterification of silanols was reported by Brinker et al [10] to proceed much faster under acid-catalyzed conditions. In alcoholic solutions at low pH the depolymerization rate is very low and the siloxane bond formed cannot be easily broken. The condensation resembles the normal reaction one would associate with a thermosetting plastic, in which functional groups still embedded within the long chains can form a chemical bond through the use of thermal heat and an appropriate catalyst. Thus resulting in a three-dimensional network structure, which leads to the characteristic gel [11].

2.5 Silicon and Titanium Rates of Hydrolysis

In order to undergo hydrolysis in a multicomponent system it is important to understand the rates of hydrolysis of the different components in solution. Since this thesis deals with sol-gels in an SiO_2-TiO_2 host, we need to know what are the different rates for the two metal alkoxides. It has been well established that the rates of hydrolysis and condensation for TEOS occurs at a slow rate, since Si is not very electropositive [41]. Ti on the other hand is highly electropositive suggesting a faster rate of hydrolysis. Since metals or metalloids of interest for membrane and catalyst formation (Si, Al, Ti, etc.) have coordination numbers (CN) $\geq$ 4, complete condensation would lead to compact, particulate oxides [40]. It is difficult to avoid particle formation for highly electropositive species such as Ti and Zr. These metals must therefore be chelated using slowly hydrolyzing multidentate ligands such as acetylacetone [42] or alcohol amines [43] to reduce both the effective functionality and the rates of hydrolysis and condensation.

2.6 Rare Earth Nitrates and Doping

Knowing the processes of hydrolysis and condensation and the catalysts used to form a sol solution, various organic solvents and how doping with a rare earth salt effects the sol solution, must be taken into consideration.

Solvents can have a significant effect on the rate of hydrolysis depending upon whether the solvent is polar or non-polar or again if one is considering acid or base catalysis. The formation of these gels can be achieved without the use of alkoxides and for reasons of economics it is often desirable to reduce the number of alkoxides in the system. In many

cases, it is possible to use metal salts provided the salts are soluble in alcohol. Typically, TEOS is used as the precursor and the alcoholic salts are added to this. This is particularly useful for Group I and II elements, which form insoluble alkoxides. The salts that are commonly used are citrates, acetates, and nitrates [11]. Chlorides and sulphates tend to be more stable than nitrates thus the anion is difficult to remove. Nitrates are the most popular salt yet they are highly oxidizing and can lead to explosions during drying if dissolved in alcoholic solutions. A study by Lochhead and Bray [37] on the spectroscopic characterization of doped sol-gel silica gels demonstrates the affinity of three different europium salts including nitrates, chlorates and perchlorates. The study shows that the NO_3^- ions have an affinity for the inner coordination sphere of Eu^{3+}, which is greater than the affinity of Cl^-. ClO_4^- ions retain an outer-sphere interaction with Eu^{3+} throughout the sol-gel process. The same study revealed that europium-nitrate based samples show an intense luminescent signal as compared to the chloride-based samples, and both had a more intense signal than the extremely weak luminescence of the perchlorate-based samples. Inner-sphere complexation of Eu^{3+} by NO_3^- in the sol is not unexpected. This is easily justified if the chemical reactions, which occur, are examined. The hydrolysis of TEOS both consumes water as a reactant and generates ethanol as a product. Since hydrolysis is rapid at low pH's under consideration, the ethanol to water ratio should increase during the early stages of the process. A high ethanol to water ratio leads to a more effective inner-sphere interaction between NO_3^- and Eu^{3+}.

Acetates have been shown to be safer and sometimes more soluble than nitrates. The only disadvantage is that these salts do not thermally degrade as well as nitrates so their removal from the gel is slightly challenging. Acetates are also basic in solution, which can

lead to a very rapid gelation of silicates, but this can always be counter acted by buffering the system with acetic acid. Once the solution has successfully been doped with a rare earth salt one can then proceed to form the gel through a drying procedure.

2.7 Drying

This process involves the removal of the majority of included solvent in the gel, which in the case of sol-gel synthesis is mainly alcohol and water. Removal of these components is essential to the final formation of the solid, which possesses a very high level of porosity. A major problem in producing gel-based optics is removal of hydroxyl groups, which are both chemi-adsorbed and physi-adsorbed. These hydroxyl groups give rise to atomic vibrational energy absorption in almost the entire range of ultraviolet to infrared wavelengths (160-4500 nm) and thus decrease the optical applications of these glasses [5]. The drying is accomplished by evaporation and Scherer [44] divides this process into several stages. First, the body shrinks to accommodate the liquid lost by evaporation, and the liquid-vapor interface remains at the exterior surface, this stage is known as the constant rate period, since the evaporation rate per unit area of the drying surface is independent of time [5]. The second stage begins when the body is too stiff to shrink, so the liquid recedes into the gel interior. Initially, a continuous liquid film remains that supports flow to the exterior, where the evaporation continues to occur. Eventually, the liquid becomes isolated into droplets, so evaporation of liquid in the gel and the diffusion of vapor to the exterior are required. Of course, the size and shape of the sample will determine the length of time of the heat treatment. If one wishes to dry a very large monolithic piece it could take as long as several months. If one wishes to produce a

powder and is not too worried about gel cracking, one would want to dry the piece as quickly as possible to ensure a lot of cracks since this will be useful to mill it down to a fine powder. Cracking is due to capillary forces and is a major factor in the drying stage. Taking capillary forces into consideration, the pores in a gel, which have a diameter in the nanometer range, must have the included liquid at a very high hydrostatic pressure. If not, these forces can act in such a way to collapse the pores, thus gels that have very fine pores will have a greater tendency to crack [11].

The secret to drying is to dry at a slow rate, which will reduce the gradient in strain allowing shrinkage to occur at comparable rates. Aging the gel can strengthen the network and in some cases increase the pore radius.

In general, it is necessary to increase pore size and reduce the forces which promote cracking therefore the method used to synthesize the gel must be examined. Referring back to section on acid and base catalysts, an acid catalyzed reaction forms gels that have tangled branched polymeric chains, which consequently form the gel. In a basic medium, the chains become highly branched before they start to entangle and begin to take on a particulate nature. A simple illustration of the two-branched systems given by Jones [11] is shown in Figure 2.7.1.

During drying of the polymeric gels, the structure compacts and further cross-links until the gel network is able to resist the surface tension forces so on further drying the porosity will appear in the structure [11]. If the bulk densities of an acid and base medium both with the same amount of water is taken into consideration, it has been observed that the acid catalyzed reaction has a greater density, 1.8 g/cm^3 whereas that of the base catalyzed is 0.8 g/cm^3 which suggests that the clusters behave as larger particles as shown in Figure

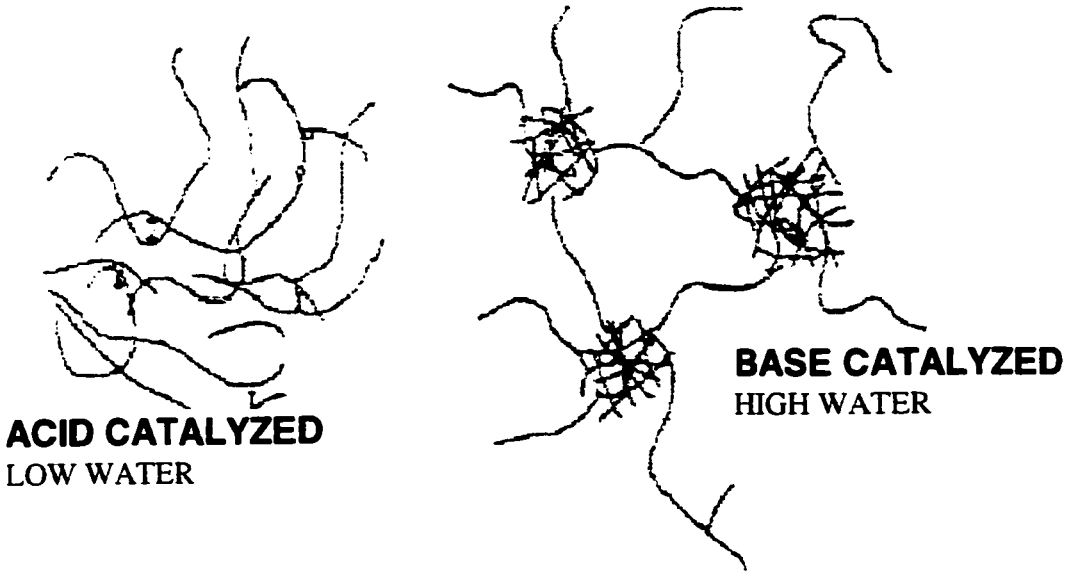

Figure 2.7.1: Branched systems for acid and base catalyzed reactions.

2.7.1, and on drying did not pack efficiently leading to the low density. In these types of gels, aging is important in order to create a very rigid structure with time, allowing the clusters to continue to coalesce.

2.8 Densification and Sintering

In this section an overview of the different heating temperatures used will be given. The different temperatures are important in order to densify the structure to produce a rigid sample that is free from rehydration stresses. Although the sample is considered "dry" up to this point, it still contains a large concentration of adsorbed hydroxyl groups as well as residual organics, which must be removed while the gel is still porous. If they were to be removed in a closed pore system, the gel can bloat and expand distorting the structure of the densified gel. The time and temperature are thus important and depend very much on the original gel structure. In contrast to traditional glass melts, the temperature range for densification is considerably lower. The driving force for this low temperature is referred to as the gel's desire to reduce surface free energy and therefore surface area.

Brinker and Scherer [45] outlined one of the most thorough studies of densification as shown in Table 2.8.1:

Table 2.8.1: Temperature ranges for the densification of sol-gels as outlined by Brinker and Scherer.

Very low temperature	Shrinkage due to capillary forces
Low temperature	Condensation polymerization increasing the number of cross-links
Near T_g	Structural relaxation decreasing the free volume thus free energy of the network
Maximum temperature	Viscous sintering to form final dense solid

Table 2.8.2 demonstrates the different temperature ranges experienced in a multicomponent borosilicate glass studied by Brinker and Scherer [45] that was densified below 700^{0}C.

Table 2.8.2 : Gel behavior as a consequence of temperature.

Temperature ^{0}C	**Regime**
25-150	Weight loss/shrinkage due to evaporation of large amounts of water and alcohol. Little gel shrinkage due to capillary forces.
150-525	Polycondensation/considerable weight loss and shrinkage due to loss of water and from oxidation of the organic residual compound. Shrinkage due to densification of network due to cross-linking and polymerization.
525-700	Large shrinkage/little weight loss. Rapid shrinkage due to viscous flow sintering where the pores in the gel collapse.

Each temperature range above has a corresponding percentage of shrinkage attributed to densification and are as follows:

Regime I: 3%
II: 32%
III: 62%

In most gels after densification at high temperatures, there are still residual amounts of water and organic groups, which are bonded as silanol groups. It is therefore important to remove as much solvent as possible before the pores begin to diminish and close in order to prevent bloating. After densification there are some pores that have not necessarily collapsed leading to scattering of light by these residual pores.

2.9 Waveguides

In order to comprehend the propagation of light within a waveguide, one must first understand the refraction and reflection of light and how these properties behave on a thin-film substrate.

Previously in Section 1.2 the three components required in order to capture the light were discussed including the cover which is usually air with an index of refraction of 1, the film with a certain thickness and index of refraction, and the substrate which is usually a glass slide with refractive index of approximately 1.46. Also mentioned, was the fact that the refractive index of the film needs to be greater than that of the substrate and cover in order to observe any type of light propagation.

In order to further understand the propagation of light, the use of Snell's law should be mentioned and is shown in equation 2.9.1.

$$n_1 \sin\theta_1 = n_2 \sin\theta_2 \tag{2.9.1}$$

Snell's law states that a reflected wave will have the same angle as that of the incident beam (θ_1) and that the refracted wave will have an angle θ_2. The incident beam has an amplitude of A and the reflected wave has an amplitude B that is related to A by a complex reflection coefficient R.

$$B = RA \tag{2.9.2}$$

The reflection coefficient depends on the angle of incidence and the polarization of the light. There are two types of polarization involved when discussing waveguides, transverse electric modes (TE) and transverse magnetic modes TM . For TE modes, the electric field is perpendicular to the plane of incidence spanned by the wave normal and the normal to the interface [20]. The following equation is used to determine the transverse electric mode taking into consideration the reflection coefficient.

$$R_{TE} = n_1\cos\theta_1 - n_2\cos\theta_2 / n_1\cos\theta_1 + n_2\cos\theta_2 = n_1\cos\theta_1 - \sqrt{n^2_2 - n^2_1\sin^2\theta_1} / n_1\cos\theta_1 + \sqrt{n^2_2 - n^2_1\sin^2\theta_1} \tag{2.9.3}$$

The formula corresponding to the transverse magnetic mode in which the magnetic fields are perpendicular to the plane of incidence is given by:

$$R_{TM} = n_2\cos\theta_1 - n_1\cos\theta_2 / n_2\cos\theta_1 + n_1\cos\theta_2 = n^2_2\cos\theta_1 - n_1\sqrt{n^2_2 - n^2_1\sin^2\theta_1} / n^2_2\cos\theta_1 + n_1 \sqrt{n^2_2 - n^2_1\sin^2\theta_1} \tag{2.9.4}$$

The critical angle, θ_c is given by Kogelnik [20] as

$$\sin\theta_c = n_2/n_1 \tag{2.9.5}$$

If $\theta_1 < \theta_c$, only partial reflection occurs and a real valued R is obtained. If the critical angle is exceeded then $|R| = 1$ and total reflection of the light occurs and R is now complex valued and a phase shift is imposed on the reflected light.

$$R = \exp(2j\phi) \tag{2.9.6}$$

The formula for the corresponding phase shifts for ϕ_{TE} and ϕ_{TM} can be written as:

$$\tan\phi_{TE} = \sqrt{n^2_1\sin^2\theta_1 - n^2_2} / n_1\cos\theta_1 \tag{2.9.7}$$

$$\tan\phi_{TM} = n^2_1\sqrt{n^2_1\sin^2\theta_1 - n^2_2} / n^2_2\, n_1\cos\theta_1 \tag{2.9.8}$$

The dependence of ϕ_{TE} on the angle of incidence θ_1 may be illustrated by using the index ratio n_2/n_1 equal to 0.7, which corresponds, approximately to the interface between air and

SiO_2. Using 0.7 as index ratio it is observed that the phase shift increases from 0 at the critical angle to $\pi/2$ at grazing incidence where $\theta_1 = 90^0$. The behavior for TM is quite similar. The example shows the behavior of light within two lossless isotropic, homogeneous dielectric media with two different types of index of refraction. The behavior of light in an "asymmetric" slab waveguide that takes into consideration three types of refraction including that of the cover, film and substrate can now be examined. In this case, two critical angles must be taken into consideration, namely θ_s which, corresponds to the total reflection from the film-substrate interface and $\theta_c < \theta_s$ which is the condition for total reflection from the film-cover interface. As the angle of incidence θ increases, three different patterns are observed as demonstrated in Figure 2.9.1. The first pattern, at small angles where $\theta < \theta_s$, θ_c light incident from the substrate side is refracted according to Snell's law and escapes through the cover. This is the radiation mode pattern since there is essentially no confinement of light. If the angle θ increases slightly such that $\theta_c < \theta < \theta_s$, then the light incident from the substrate is refracted at the film-substrate interface, totally reflected at the film-cover interface, refracted back into the substrate through which the light escapes from the structure [20]. There is no confinement of light and this pattern is referred to as the substrate radiation mode. When the angle is large enough, and total internal reflection occurs at both interfaces, where θ_s, $\theta_c < \theta$, the light is trapped inside and confined by the film and propagates in a zig-zag fashion. This pattern is known as the guided mode pattern.

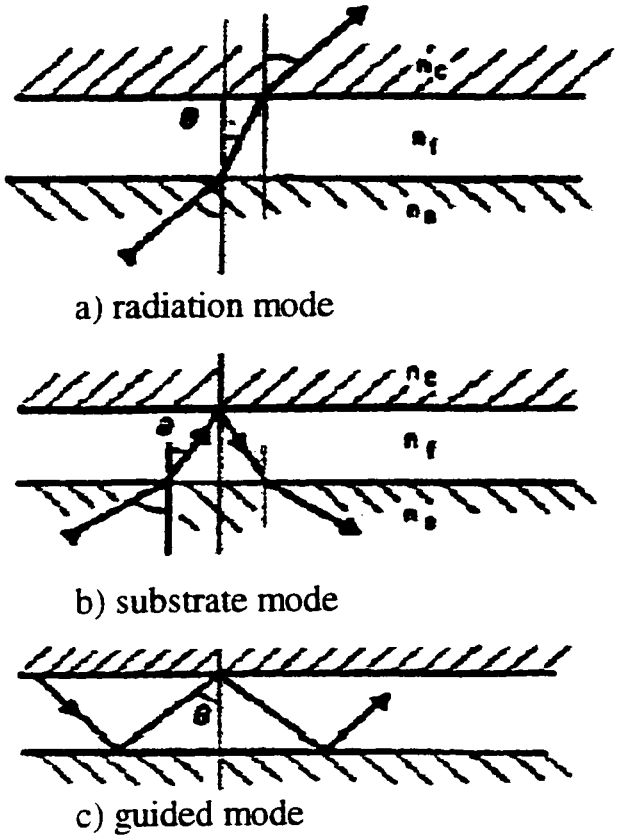

Figure 2.9.1: Wave pictures for the different propagation modes;
a) radiation mode, b)substrate mode, and c) guided mode.

These guided modes are what we are most interested in and will be the focus of the following section.

The waves discussed above are monochromatic with an angular frequency ω, with wavelength λ, and they travel with a wave vector $\mathbf{k}n_f$ (n_f = index of refraction in the film) in the direction of the wave normal where the absolute value of $\mathbf{k}$ is:

$$k = \frac{2\pi}{\lambda} = \frac{\omega}{c} \tag{2.9.9}$$

Where c is the speed of light in a vacuum. The field of these waves, vary as:

$$\exp\,[-jkn_f(\pm x\cos\theta + z\sin\theta)] \tag{2.9.10}.$$

For a guided mode, the zig-zag pattern predicts a propagation constant β and the related phase velocity v_p:

$$\beta = \omega/v_p = kn_f \sin\theta, \tag{2.9.11}$$

which is the z-component of the wave vector $\mathbf{k}n_f$. However, not all angles θ are allowed; only a discrete set of angles lead to a self-consistent picture that corresponds to what is known as "guided modes" [20].

2.9.1 Goos-Hanchen Shift

This section touches upon the flow of energy within the asymmetric slab waveguides and how this energy flow is important to understanding the behaviour of energy within the guide. In order to understand this energy flow a definition of a light ray must be given. A light ray is defined as the direction of the Poynting vector or the energy flow of light. Consistent with this is the view of a ray as the axis of narrow beam of light or wave

packet [20]. If the case of a simple system of a plane wave in an isotropic homogeneous medium is taken, the direction of the ray and wave normal are generally the same, however, in an anisotropic medium, the ray generally points in a different direction from that of the wave normal.

The Goos-Hänchen shift is a perfect example of this different ray and wave behavior. This shift occurs upon total reflection from a dielectric interface. More specifically, the reflected ray B is shifted laterally relative to the incident ray or wave packet A[20]. The shift may be calculated by using the following equations, and the equation is given for the lateral ray shift in the substrate shown as $2z_s$

$$A = [\exp(j\Delta\beta_z) + \exp(-j\Delta\beta_z)]\exp(-j\Delta\beta_z) \qquad (2.9.1.1)$$

$$= 2\cos(\Delta\beta_z)\exp(-j\beta_z) \qquad (2.9.1.2)$$

Before applying the laws of reflection (section 2.9) to each individual wave, note that the phase shift occurring upon total reflection is a function of θ (and β). For small $\Delta\phi$ and $\Delta\beta$, an expansion of the following form can be used

$$\phi(\beta + \Delta\beta)\ \phi(\beta) + (d\phi/d\beta)\ \Delta\beta \qquad (2.9.1.3)$$

Using equation 2.9.1.3, the amplitude B (z) of the reflected wave packet at x = 0 is obtained

$$B = \{\exp[j(\Delta\beta_z - 2\Delta\phi)] + \exp[-j(\Delta\beta_z - 2\Delta\phi)]\}\exp[-j(\beta_z - 2\phi)] \qquad (2.9.1.4)$$

$$= \cos[\Delta\beta(z-2z_s)]\ \exp[-j(\beta_z - 2\phi)]\ , \qquad (2.9.1.5)$$

where

$$z_s = d\phi/d\beta \qquad (2.9.1.6)$$

Equation 2.9.1.6 gives the lateral shift of the wave packet. Using equations 2.9.11, 2.9.7 and 2.9.8 kz_s for the TE modes is given as

$$kz_s = (N^2 - n_s^2)^{-1/2}\tan\theta \qquad (2.9.1.7),$$

and for the TM modes as

$$\frac{kz_s = (N^2 - n_s^2) - 1/2\tan\theta}{\frac{N^2}{n_s^2} + \frac{N^2}{n_f^2} - 1} \qquad (2.9.1.8)$$

The light is shifted in the cover and substrate and there is a penetration of the ray in both the cover and substrate given as x_s in the substrate and x_c in the cover. The light penetrates to a depth of x_s into the substrate before being reflected back into the structure. The depth x_s in the substrate is given as:

$$x_s = \frac{z_s}{\tan\theta} \qquad (2.9.1.9)$$

The light propagation and Goos-Hanchen shift is shown in Figure 2.9.1.1.

In addition to the shift and ray penetration in both the cover and substrate, a thickness of the overall film known as h effective (h_{eff}) is developed which takes into consideration the ray penetration. The thickness of the film originally is given as h, the new thickness or "effective guide thickness" is equal to the original thickness of the film plus the ray penetration in the cover and substrate

$$h_{eff} = h + x_s + x_c \qquad (2.9.1.10)$$

This thickness is obviously larger than that of the original film, and the light that spreads into the cover and substrate are essentially confined to this effective guide thickness.

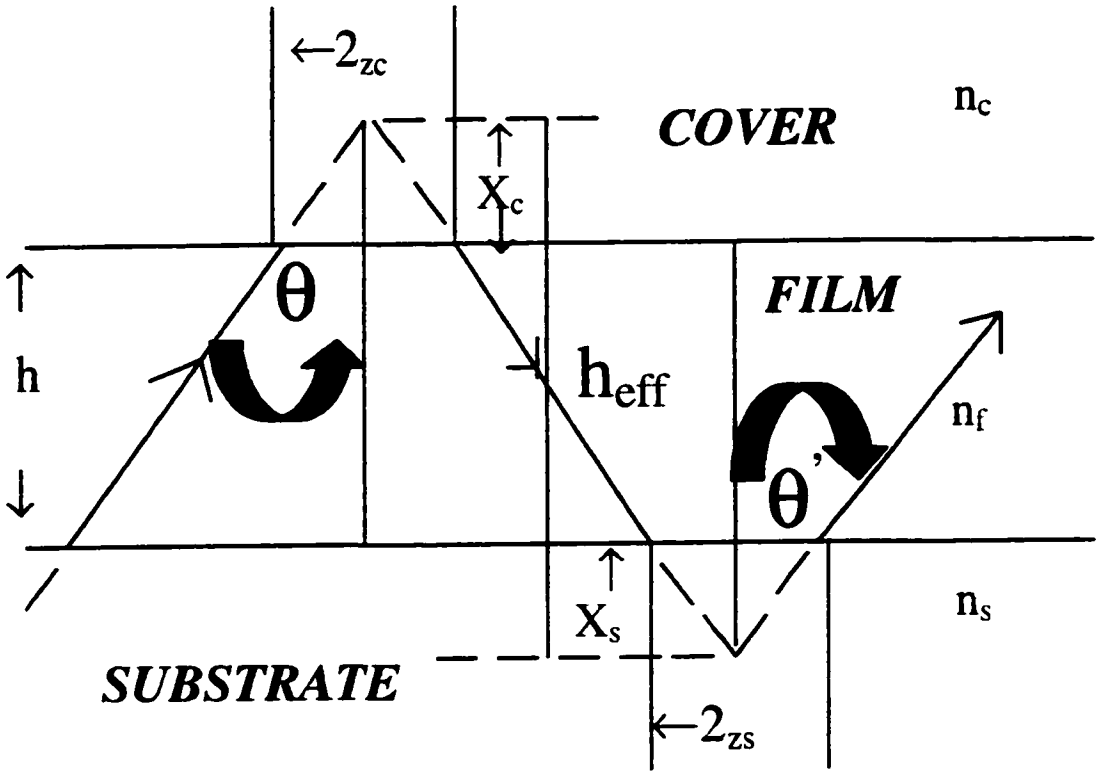

Figure 2.9.1.1. : Ray picture of zig-zag light propagation in a slab waveguide.
Seen in diagram is Goos-Hanchen shift and effective guide thickness.

2.10 Energy Levels Of The 4*f* Electrons and Selection Rules

An electron in a many electron atom such as europium or terbium, experience a Coulombic repulsion from all other electrons present. This Coulombic interaction as well as spin orbit matrix calculations aid in determining the energy levels of the atom. The following Hamiltonian is used to determine the 4*f* energy levels [46]:

$$H = \frac{\hbar}{2m}\sum_{i=1}^{N}\nabla_i^2 - \sum_{i=1}^{N}\frac{Ze^2}{r_i} + \sum_{i<j}^{N}\frac{e^2}{r_{ij}} + \sum_{i=1}^{N}\xi(r_i)\frac{s_i}{i} \qquad (2.10.1)$$

Where m is the electronic mass, ∇i^2 is the Laplacian operator (d/dx + d/dy + d/dz), Z is the charge on the nucleus, e is the electronic charge, r_i is the distance of the electron from the nucleus, r_{ij} is the distance between electron i and electron j, $\xi(r_i)$ is the spin orbit coupling function $\underline{s_i}$ and $\underline{l_i}$ are the spin and orbital angular momenta for the electron i respectively. The first two terms in the Hamiltonian represent the kinetic energy ($-\hbar^2 / 2m\sum_{i=1}^{N}\nabla_i^2$) and the Coulombic interaction ($\sum_{i=1}^{N} Ze^2 / r_i$). These two terms do not remove the degeneracy of the 4*f* energy levels and thus can be ignored. The last two terms determine the energy level structure for the 4*f* electrons and thus are important.

The term $\sum e^2/r_{ij}$ splits the energy of the $4f^n$ configuration into different Russell Saunders terms. When there are several electrons outside a closed shell the coupling of all the spins and the orbital angular momenta must be considered. This approximation may be used when the spin-orbit coupling is weak, and therefore all the orbital angular

momenta of the electrons couple to give a total L and all spins couple to give a total S. The value of L describes the magnitude of the angular momentum through $(L\ (L+1))^{1/2}\hbar$. The J values are therefore determined as follows:

$$J = L+S,\ L+S-1,\ldots\ |L-S| \qquad (2.10.2)$$

The values of L are shown below:

L: 0 1 2 3 4 5 6 ...

S P D F G H I...

The probability that a transition will occur between states a and b depends on the matrix element given as $\langle b|\ \mu\in\ |a\rangle$ where $\mu\in$ is the appropriate operator. Since electric dipole transitions have $\mu\in$ as odd, then they are referred to as ungerade. The parity of the final state therefore must be different then that of the initial state. This property is known as Laporte's rule which give rise to the selection rules for the electric dipole transitions, which are given below:

$$\Delta l = \pm 1$$
$$\Delta L = \leq 6$$
$$\Delta S = 0$$
$$\Delta J \leq 6 \text{ (if } J \text{ or } J' = 0 \text{ then } |\Delta J| = 2,\ 4,\ 6)$$

Electric dipole transitions within f^n configurations become parity allowed due to the admixing of states. These selection rules are thus determined strictly from the local site-symmetry of the ion. All point groups possessing low site-symmetry for *f-f* transitions are allowed transitions and thus the only factor to take into consideration is the relative magnitude of the contribution from each dipole process.

Magnetic dipole transitions while parity allowed, due to the fact that the $\mu\epsilon$ operator is even are known as gerade and follow the rules below:

$$\Delta l = 0$$
$$\Delta S = 0$$
$$\Delta L = 0$$
$$\Delta J = 0, \pm 1 \quad (\text{not } 0 \leftrightarrow 0)$$

Thus these transitions are allowed within the $4f^n$ configurational states. In this thesis, the transitions belonging to europium and terbium are of interest. Table 2.10.1 demonstrates the allowedness of the optical transitions for the two ions.

Table 2.10.1: Allowed and forbidden transitions for Eu^{3+} and Tb^{3+} based on the selection rules.

Transition	Allowedness
$^5D_0 \rightarrow {}^7F_0$ (Eu^{3+})	Forbidden
$^5D_0 \rightarrow {}^7F_1$ (Eu^{3+})	Magnetic dipole allowed
$^5D_0 \rightarrow {}^7F_2$ (Eu^{3+})	Electric dipole allowed
$^5D_0 \rightarrow {}^7F_3$ (Eu^{3+})	Forbidden
$^5D_0 \rightarrow {}^7F_4$ (Eu^{3+})	Electric dipole allowed
$^5D_4 \rightarrow {}^7F_5$ (Tb^{3+})	Magnetic dipole allowed
$^5D_4 \rightarrow {}^7F_4$ (Tb^{3+})	Forbidden
$^5D_4 \rightarrow {}^7F_3$ (Tb^{3+})	Magnetic dipole allowed
$^5D_4 \rightarrow {}^7F_2$ (Tb^{3+})	Electric dipole allowed

2.11 Energy Transfer

The energy transfer from an excited ion (donor) to an unexcited ion (acceptor) generally occurs in three steps. The three steps are outlined below:

1. Absorption of a photon by the donor ion
2. Energy transfer from donor to acceptor
3. Emission of a photon by the acceptor

In general there are two types of energy transfer processes namely, nonradiative and radiative.

The nonradiative processes provide an additional decay mechanism to the donor and thus the lifetime of the donor is shorter. This is mainly due to the van der Waals interactions between the two ions. Since these interactions are fairly weak, no drastic changes in the energy levels of the donor and acceptor ions is observed [47].

Nonradiative energy transfer can be divided into two types, resonant and nonresonant transfer. In resonant transfer mechanisms first formulated by Forster [25] in 1948, the energy transfer involves electric dipole-dipole interactions for organic molecules.

Dexter [26] a few years later modified Forster's theory to include forbidden transitions allowing for the study between dopant ions in inorganic solids. In resonant energy transfer, an excited donor ion decays down to the ground state and transfers a portion of its energy to the unexcited acceptor ion without creating or destroying any phonons or photons.

Nonresonant energy transfer on the other hand involves the mismatch of energy between two ions, which is thus compensated by the simultaneous emission or absorption of one or

more phonons. The phonons, assist to fill the energy gap and is thus termed a phonon-assisted energy transfer process.

Radiative processes unlike nonradiative processes proceed by a photon being emitted by the donor ion and is thus absorbed by the acceptor ion. Here, the donor is unaffected and the energy transfer is efficient when the acceptor ion has a very strong absorption in the general area where the donor emits. The Radiative processes also can be divided into two sequential steps in which primarily, the donor ion in an excited state will decay to the ground state and emits a photon. Secondly, the acceptor ion will absorb this emitted photon. The quantum yield of this transfer of energy can be given by the following equation:

$$\eta_T(E) = A\nu\int f_D(E)\,[1-e^{-C+CA\lambda\sigma A}(E)]dE \qquad (2.11.2)$$

where the average is taken over the linear dimension λ, $v = (3/4)\pi R^3$ and $f_D(E)$ = normalized shape of the donor transition, $\sigma_A(E)$ = absorption cross section of the acceptor, C^+ = density of the available activator sites, and C_A = concentration of the acceptor ion [27].

There are five stages that occur in order to observe any type of transfer process as demonstrated in Figure 2.11.1. The first involves absorption of a photon of energy approximately equal to E_o by the donor. In the second step there is a relaxation of the lattice that surrounds the donor ion by a certain quantity in which the available electronic energy in a radiative transition from the donor is $E_1<E_0$. The third step demonstrates the transfer of energy from E_1 to the acceptor ion. The fourth step occurs in two stages: relaxation around the acceptor such that the available electronic energy in the radiative transition is $E_2<E_1$, followed by relaxation around the donor to a state similar but not

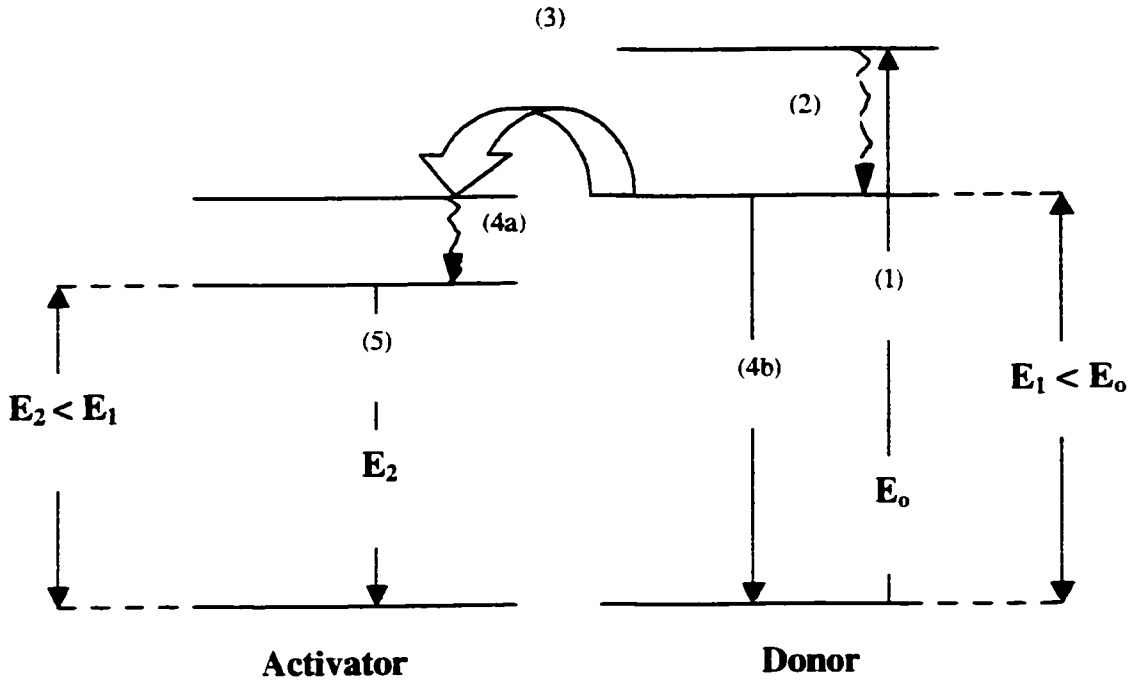

Figure 2.11.1: Schematic diagram of the five major stages involved in an energy transfer process.

identical to its original unexcited state. The last step is therefore emission of the energy from E_2 to the acceptor ion.

Each stage can be further divided into five steps that indicate the relative time scale for each process. The first step is dependant on the pump source an is therefore in the nano range. The second step occurs in about 10^{-13} seconds or more and the excess energy is released by the lattice as phonons. The third step is dependant on the distance between the surrounding acceptor ions however there are exceptions when the distance is greater than 10Å where the following is expected to occur:

(i) as a photon which may or may not be absorbed by an acceptor atom depending on its absorption cross section and on the total number of acceptor ions present in the crystalline system

(ii) as a photon which may be reabsorbed by another donor, depending on whether or not the absorption and emission bands of the donor overlap and upon the total number of donor ions in the crystal

(iii) as electronic excitation energy E_1 on a different donor atom without a photon as a intermediary, depending on the concentration of the donor and on the overlap between the emission and absorption bands of the donor

(iv) as thermal energy following a nonradaitive process

The fourth step occurs at a time $\geq 10^{-13}$ seconds and the fifth and final step requires a time of 10^{-8} seconds or longer depending on the forbideness of the transition [48].

CHAPTER 3

3.0 EXPERIMENTAL

3.1 Sample Preparation

Europium and terbium doped sol-gels were prepared by the combination of two different solutions. The first solution consisted of tetraethyorthosilicate (TEOS), water, isopropanol, HCl, and either europium nitrate pentahydrate or terbium nitrate hexahydrate. A 100 ml round bottom flask was used in which 8 ml's of isopropanol was mixed with 10µl of HCl. 1.90 ml's of water (hydrolyzing agent) was then added slowly to prevent precipitation due to the differences in hydrolyzing rates of the multicomponent system. The solution was left to react for 10 minutes before the addition of the rare earth nitrates. The solution was then left to stir for approximately 15 minutes or until the rare earth solid had completely dissolved. TEOS is the last addition for solution one in which 6 ml's were added in a drop-wise fashion again to prevent any precipitation within the sol. Solution 1 was left to stir for approximately 30 minutes during which time the second solution was prepared. The second solution consisted of 4 ml's of Ti (IV)Isopropoxide, which was chelated using 2 ml's of glacial acetic acid. The two solutions were then combined and diluted to equal volume with 22 ml's of spectrograde methanol. The final solution was left to react for a few minutes before taking the pH. The sols were then cast in 50 mm diameter X 15 mm height petri dishes covered and sealed with tape in order to make it as air tight as possible. The samples were then heated overnight in an oven between 60-70^{0}C and were further dried at no more than 200^{0}C for 15 minutes. Deuterated samples were prepared in a similar fashion in which D_2O was substituted for H_2O. The ratios used for each reagent are as follows:

Solution 1: $Si(OC_2H_5)_4 : CH_3CHOHCH_3 : H_2O : HCl$

4 :1 : 1 :0.03

Solution 2: $Ti[OCH(CH_3)_2]_4 : CH_3COOH$

2 : 1

Sol-gels were prepared at a doping concentration ranging from 1 to 5 mol% for both europium and terbium doped samples. Co-doped samples, used for the energy transfer studies were prepared by keeping constant the concentration of the donor ion (terbium) at 3 mol% and varying the concentration of the acceptor ion (europium) between 1 and 5 mol%.

3.2 Waveguide Preparation

Waveguide preparation requires that the sol be prepared as stated above. In this thesis, a 5 mol% Eu^{3+} doped waveguide was analyzed. The waveguide was prepared using the dip-coating method, in which the substrate (glass slide 80 mm in length) is dipped into the sol solution at a constant speed of approximately 50 mm/min for about 30 cycles. The apparatus used for the dip-coating method is made up of a motor that has continuous cycles and can hold a beaker with a glass slide that is fastened above it. The motor sends the glass slide in an up and down motion coating the glass slide in the sol solution. The apparatus is shown in Figure 3.2.1. Once coated, the substrates were heated in an oven at 100^0C for approximately 1 hour in order to ensure that the film has densified.

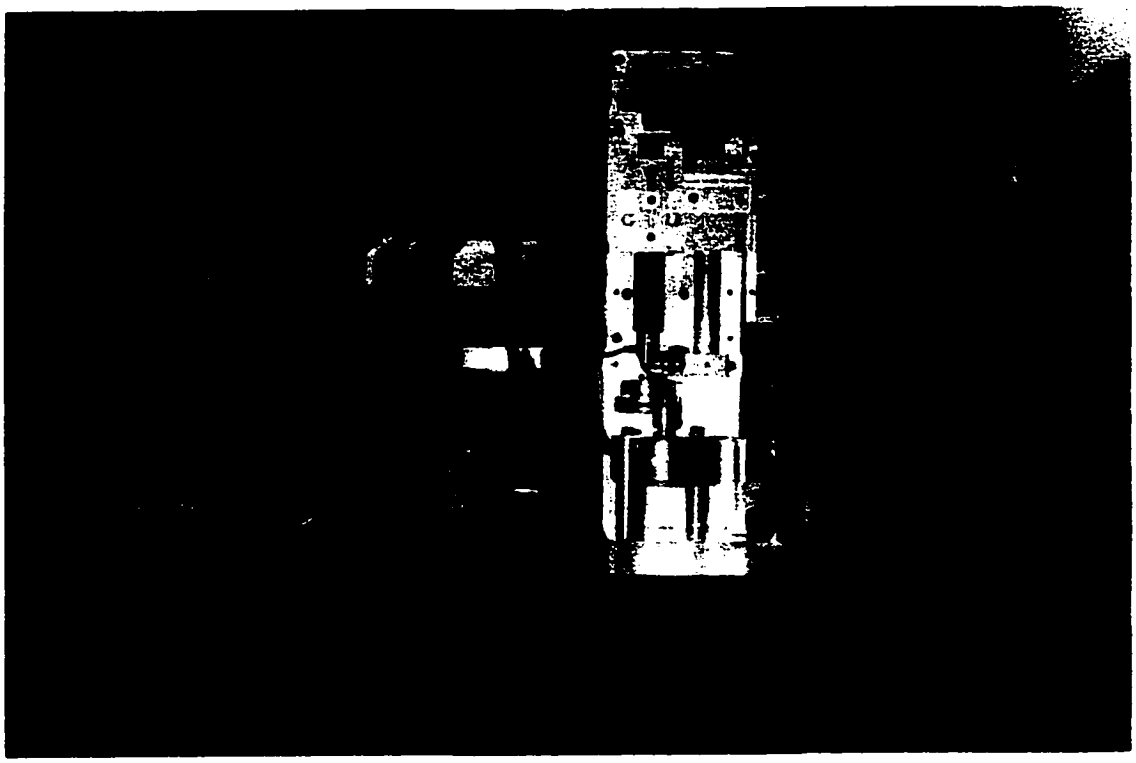

Figure 3.2.1: Apparatus for the dip-coating method.

3.3 Emission spectra

A Coherent CR-18, 20 W argon laser at an excitation wavelength of 488 nm was used to obtain emission spectra. The spectra were collected using a Jarrel-Ash 1 m Czerny Turner double monochromator with a maximum slit width of 200 um. The gratings are mounted on a cosecant bar driven by a stepper motor with a step of 0.01 cm^{-1}/pt. The signals were monitored with a thermoelectrically cooled RCA C31034-02 photomultplier tube with a flat spectral response from 200-850 nm. The photomultiplier signals were processed by a preamplifier model SR440 Stanford Research System. The spectroscopic hardware is interfaced to the computer through a gated photon counter Model SR 400 Stanford research Systems data acquisition system. The signals were recorded under computer using the Stanford SR 465 software data acquisition/analyzing system. Fluorescence lifetimes were measured upon excitation with the 488 nm line of the argon laser. The excitation light was modulated by a chopper SR540 Stanford Research System and lifetimes were recorded using a gated photon counter. FT-IR spectra were recorded using a Nicolet Magna IR Model 550 spectrometer with a DTGS KBr detector and a KBr beamsplitter. Samples of commercial SiO_2, TiO_2 and all sol-gels were diluted with KBr and ground to a fine powder to make a pellet. The laser source in the Magna-IR system optical bench is a nominal 1 milliwatt continuous 632.8 nm laser head. The spectral range is between 4000-400 cm^{-1} and all spectra were collected in the transmittance mode using the computer based software of Omnic™ version 3.1. Raman spectra were recorded using a Jarrel-Ash 1 m monochromotor at excitation wavelengths of 457.98 nm, 496.43 nm, and 514.5 nm using the argon laser. Light scattered at $\pi/2$ from the incident beam was

monitored with an RCA C31034-02 photomultiplier operating in the photon counting mode.

Low temperature emission spectra and energy transfer studies at 77K were performed using an Oxford Instruments continuous flow cryostat (CF 204) with an excitation wavelength of 488 nm line using the argon laser. The waveguide emission spectra were measured at an excitation wavelength of 514.5 nm from a Coherent CR-18, 20 W argon laser.

A schematic illustration of the laser lab is shown in Figure 3.3.1.

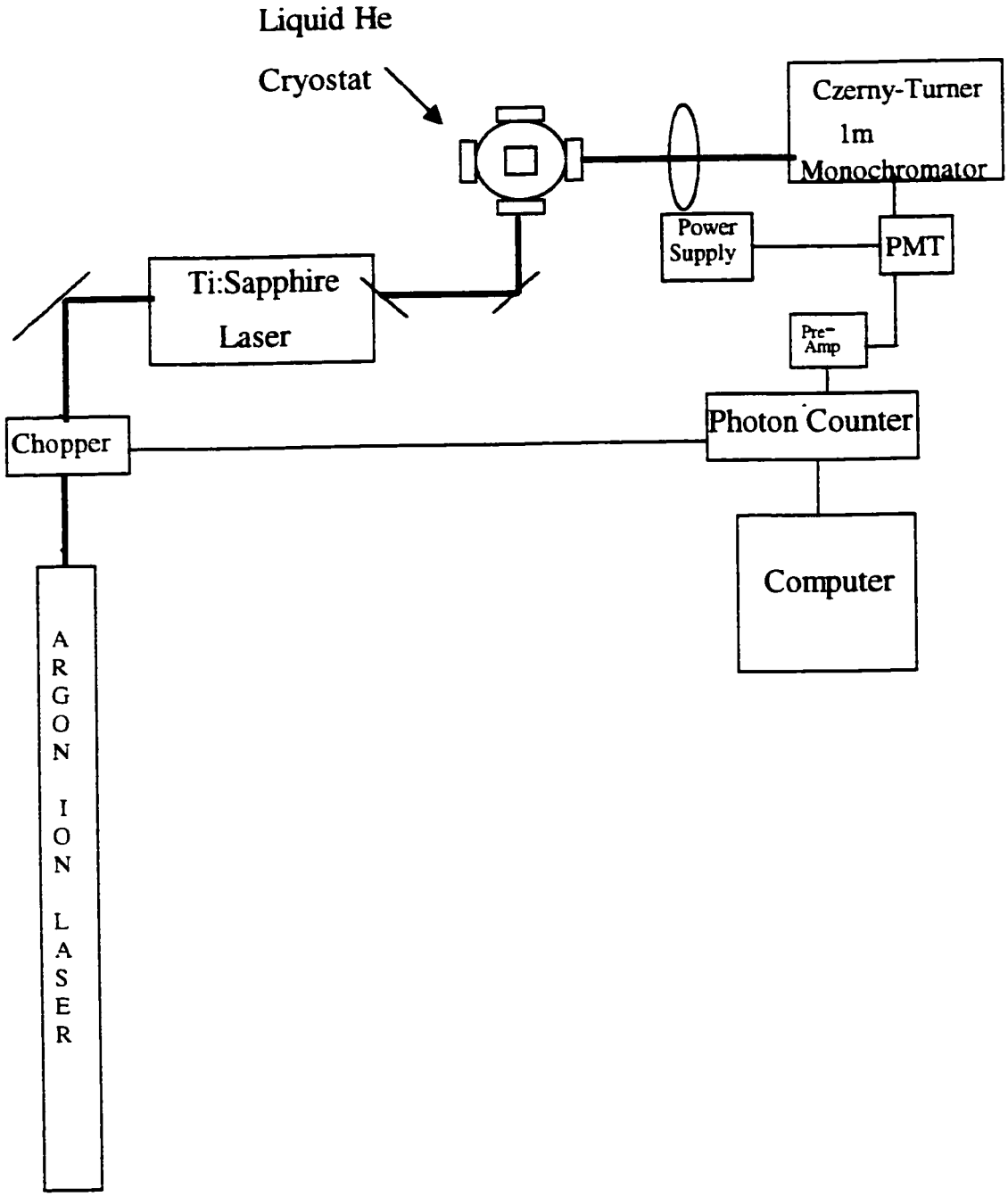

Figure 3.3.1 : Schematic arrangement of the apparatus for the measurement of the emission spectra and decay times.

CHAPTER 4

4. Results and Discussion

In this thesis, the energy levels for Eu^{3+} and Tb^{3+} were investigated within an SiO_2-TiO_2 sol-gel host. The energy transfer mechanism between the 3 mol% Tb^{3+} and 3 mol% Eu^{3+} codoped sample, and the waveguide emission for the 5 mol% Eu^{3+} doped sample were also investigated. Infrared and Raman studies were performed in order to provide structural information of the overall sol-gel network.

This chapter is divided into eight different sections. The first and second sections show the transitions observed for Eu^{3+} and Tb^{3+} respectively at an excitation wavelength of 488 nm and 298K within the SiO_2-TiO_2 host. The third section shows the emission spectra obtained at both 298K and 77K for the codoped samples. The fourth describes all stretches and vibrations from infrared and Raman experiments at 298K. The fifth section compares the use of H_2O and D_2O as hydrolyzing agents. The sixth describes the energy transfer mechanism between Tb^{3+} and Eu^{3+}. The seventh section shows the emission obtained for the 5 mol% Eu^{3+} doped SiO_2-TiO_2 waveguide as well as the zig-zag light propagation along the length of the glass slide. The last section gives an overall representation of the structure of the sol-gel network.

4.1 Emission Spectroscopy of Eu^{3+}

Figure 4.1.1 shows the room temperature emission spectra excited at 488 nm for the Eu^{3+} doped SiO_2-TiO_2 sol-gel at concentrations from 1-5 mol%. At this wavelength, the $^5D_1$ level is excited yet no emission is observed from this level due to non-radiative processes

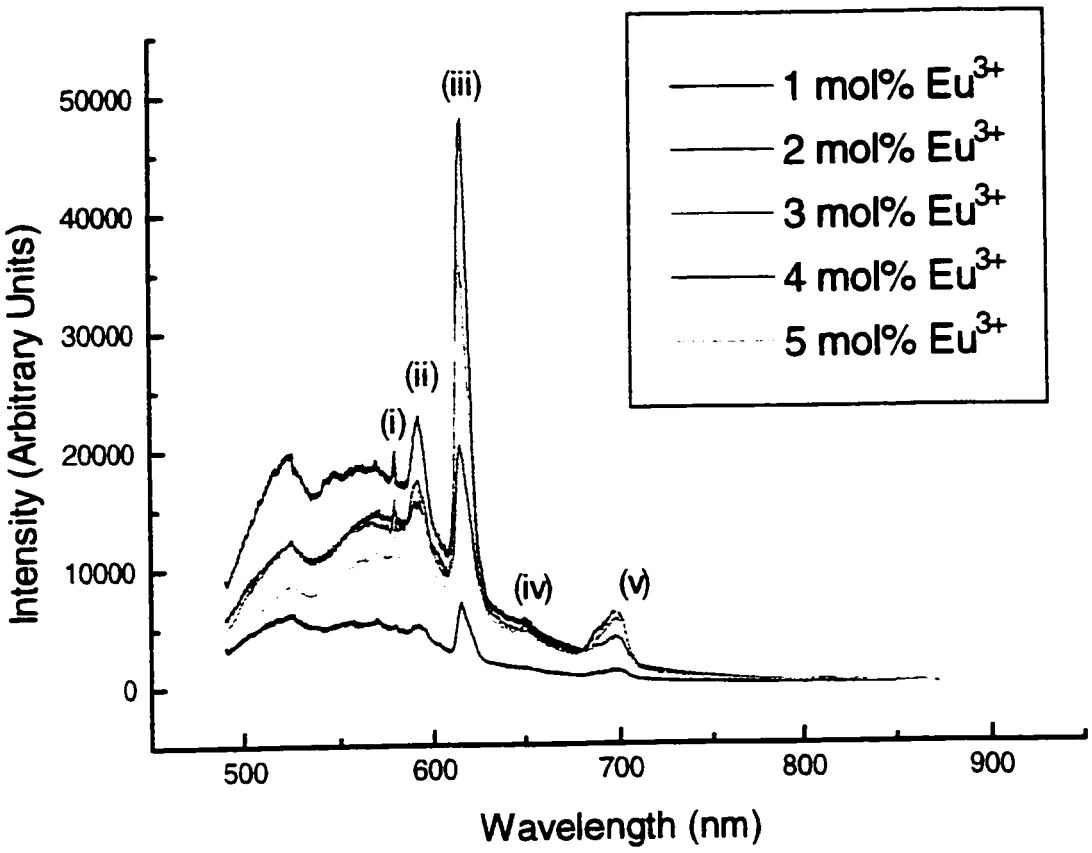

Figure 4.1.1: Emission spectra for the 1-5 mol% Eu^{3+} doped SiO_2-TiO_2 sample upon 488 nm excitation and room temperature: (i) $^5D_0 \rightarrow {}^7F_0$, (ii) $^5D_0 \rightarrow {}^7F_1$, (iii) $^5D_0 \rightarrow {}^7F_2$, (iv) $^5D_0 \rightarrow {}^7F_3$ and (v) $^5D_0 \rightarrow {}^7F_4$.

which, populate the $^5D_0$ level from which emission occurs to the lower lying ^7F_J levels. Bands were observed in the 580, 590, 625, 650, and 700 nm region of the spectrum and they can be attributed to the following transitions: $^5D_0 \rightarrow {}^7F_0$, $^5D_0 \rightarrow {}^7F_1$, $^5D_0 \rightarrow {}^7F_2$, $^5D_0 \rightarrow {}^7F_3$, $^5D_0 \rightarrow {}^7F_4$, respectively. Important features attributed to Eu^{3+} spectra include the $^5D_0 \rightarrow {}^7F_0$ transition, which is completely non-degenerate and cannot be split by a crystal-field, and the hypersensitive peak ($^5D_0 \rightarrow {}^7F_2$), which shows a strong emission in the red at approximately 615 nm. Another important feature is the anomalous behavior of the intensity ratio between the $^5D_0 \rightarrow {}^7F_1$ and $^5D_0 \rightarrow {}^7F_2$ transitions. This ratio has been used to measure the symmetry of the Eu^{3+} surroundings. The smaller the ratio, the more symmetric the site [49]. Considering the fact that the difference between the intensities of the two peaks is approximately 1:2 for $^5D_0 \rightarrow {}^7F_1$ and $^5D_0 \rightarrow {}^7F_2$ respectively, the site can be characterized as highly asymmetric. Spectra for all concentrations were found to be similar. The broad band that appears at approximately 525 nm in all spectra is the result of a water vibration since the Raman vibration for OH is at approximately 30 nm off the laser line. Since the lifetime of the $^5D_0$ level is a sensitive probe of local structure, particularly in the case of Eu^{3+} ions in the presence of hydroxyl groups, we can see in Table 4.1.1 that the decay times at this level measured for the hypersensitive peak (for all the concentrations of Eu^{3+}) are slightly shorter than that of a conventional silicate glass at 2.3 ms [50]. This phenomenon is due to the fact that OH vibrations cover the energy gap between the $^5D_1$ and $^5D_0$ level inducing non-radiative transitions that result in shorter decay times. Also, increasing the concentration of europium induces energy transfer between europium ions causing quenching of the signal since the number of europium ions per unit volume

Sample	H_2O – Acid Catalyzed Lifetime (μs) 298K
1 mol% Eu	1127
2 mol% Eu	1114
3 mol% Eu	731
4 mol% Eu	730, 390
5 mol% Eu	802
1 mol% Tb	1012
2 mol% Tb	1027
3 mol% Tb	1001
4 mol% Tb	1167
5 mol% Tb	956
3 mol% Tb 1 mol% Eu	924
3 mol% Tb 2 mol% Eu	1277
3 mol% Tb 3 mol% Eu	853
3 mol% Tb 4 mol% Eu	782
3 mol% Tb 5 mol% Eu	964

Table 4.1.1: Lifetimes of the $^5D_0 \rightarrow {}^7F_2$ transitions for Eu^{3+} and lifetimes of the $^5D_4 \rightarrow {}^7F_5$ transition for Tb^{3+} doped SiO_2-TiO_2 sample upon 488 nm excitation at room temperature.

increases with increasing concentration again resulting in a shorter decay time as shown in Table 4.1.1. The water band at approximately 525 nm is more evident in the 1 mol% sample than in all the others. An explanation of this is given by Armellini et al, [51] who observed that with low concentrations of Pr^{3+} and high H_2O content, the probability of non-radiative transitions is greater since a single O-H stretching mode instead of three Si-O stretching modes covers the energy gap.

Low temperature studies carried out at 77 K for the 3 mol% Eu^{3+} doped sample at an excitation wavelength of 488 nm gave rise to one large broad band as seen in Figure 4.1.2. This broad band (520-580 nm) is due to the fact that at low temperatures, the non-radiative process that occurs from the $^5D_1$ level to the $^5D_0$ level is cutoff. Thus no emission occurs from the $^5D_0$ level to the lower lying levels. The broad band is therefore due to OH vibrations originating from water content within the sample.

4.2 Emission Spectroscopy of Tb^{3+}

The room temperature emission spectra at an excitation wavelength of 488 nm for Tb^{3+} doped SiO_2-TiO_2 sol-gel at Tb^{3+} concentrations between 1 and 5 mol% are shown in Figure 4.2.1. Bands can be found at 543, 583, 621, and 643 nm region of the spectrum. The bands are attributed to the following transitions: $^5D_4 \rightarrow {}^7F_5$, $^5D_4 \rightarrow {}^7F_4$, $^5D_4 \rightarrow {}^7F_3$ and $^5D_4 \rightarrow {}^7F_2$ respectively. Similar to the europium samples, the terbium samples were also doped at concentrations of 1, 2, 3, 4, and 5 mol% of Tb^{3+}. An important feature attributed to Tb^{3+} spectra is the strong green emission at approximately 543 nm, which corresponds to the $^5D_4 \rightarrow {}^7F_5$ transition. Tb^{3+} emission is also known to have a blue

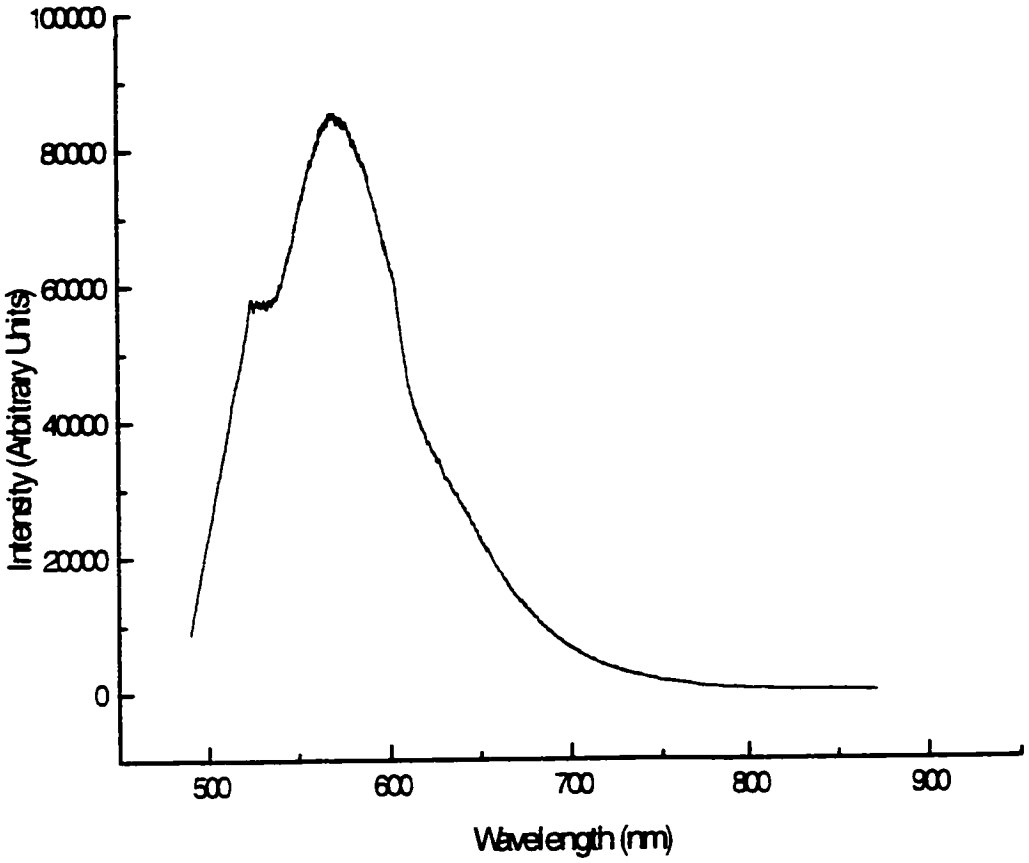

Figure 4.1.2: Emission spectra for the 3 mol% Eu^{3+} doped SiO_2-TiO_2 sample upon 488 nm excitation at 77K.

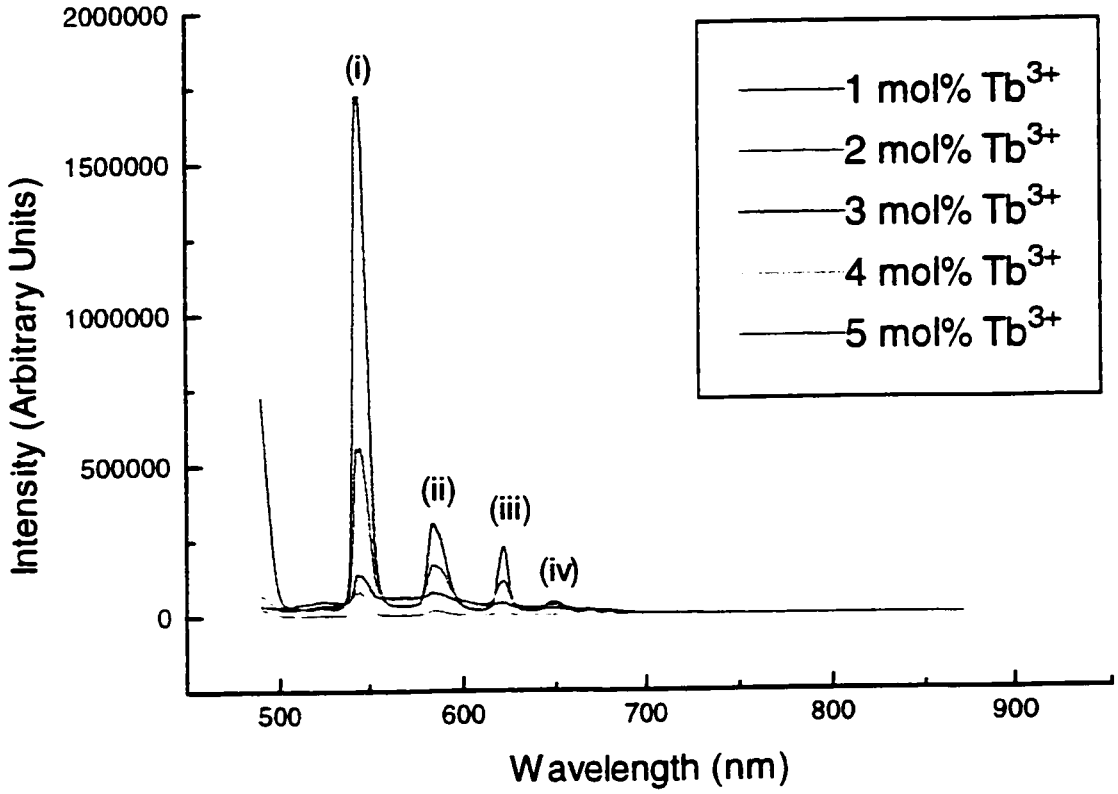

Figure 4.2.1: Emission spectra for the 1-5 mol% Tb^{3+} doped SiO_2-TiO_2 sample upon 488 nm excitation and room temperature; (i) $^5D_4 \rightarrow {}^7F_5$, (ii) $^5D_4 \rightarrow {}^7F_4$, (iii) $^5D_4 \rightarrow {}^7F_3$ and (iv) $^5D_4 \rightarrow {}^7F_2$.

emission that competes with the green emission originating from the $^5D_3 \rightarrow {}^7F_5$ level. At low Tb^{3+} concentrations ($\leq$ 1 mol%), emission from both of the excited states are observed in most Tb^{3+} activated phosphors. At relatively high Tb^{3+} concentrations ($\geq$ 2 mol%), most of the ions in the $^5D_3$ level relax non-radiatively to the $^5D_4$ level.

The spectra obtained at 298K and excitation wavelength of 488 nm for both Eu^{3+} (Figure 4.1.1) and Tb^{3+} (Figure 4.2.1) doped SiO_2-TiO_2 samples show an OH vibration present at approximately 525 nm. The method of preparation for both Eu^{3+} and Tb^{3+} doped samples is the same and therefore each sample should contain the same amount of water. If water is present within the sample after heat treatment, an OH vibration should be observed in the emission spectra at approximately 525 nm. The spectra for the Tb^{3+} doped samples (Figure 4.2.1) show that the OH vibration at 525 nm is present but not as apparent as for the spectra obtained for the Eu^{3+} doped samples (Figure 4.1.1). This is due to the fact that the OH vibrations fill the energy gap between the energy levels belonging to the europium ion and thus a non-radiative process occurs. In comparison, Tb^{3+} doped samples at an excitation wavelength of 488 nm, experience direct excitation into the $^5D_4$ level and show no evidence of non-radiative processes.

Similar to the 1 mol% Eu^{3+} doped sample, the 1 mol% Tb^{3+} doped sample also demonstrates an intense OH vibration at 525 nm as compared to the other Tb^{3+} doping concentrations which again can be correlated to the fact that there is a single O-H stretch. Decay times for the different concentrations of Tb^{3+} are shown in Table 4.1.1.

Figure 4.2.2 shows the low temperature spectra at 77K for the 3 mol % Tb^{3+} doped sample at an excitation wavelength of 488 nm. Unlike the 3 mol % Eu^{3+} doped sample,

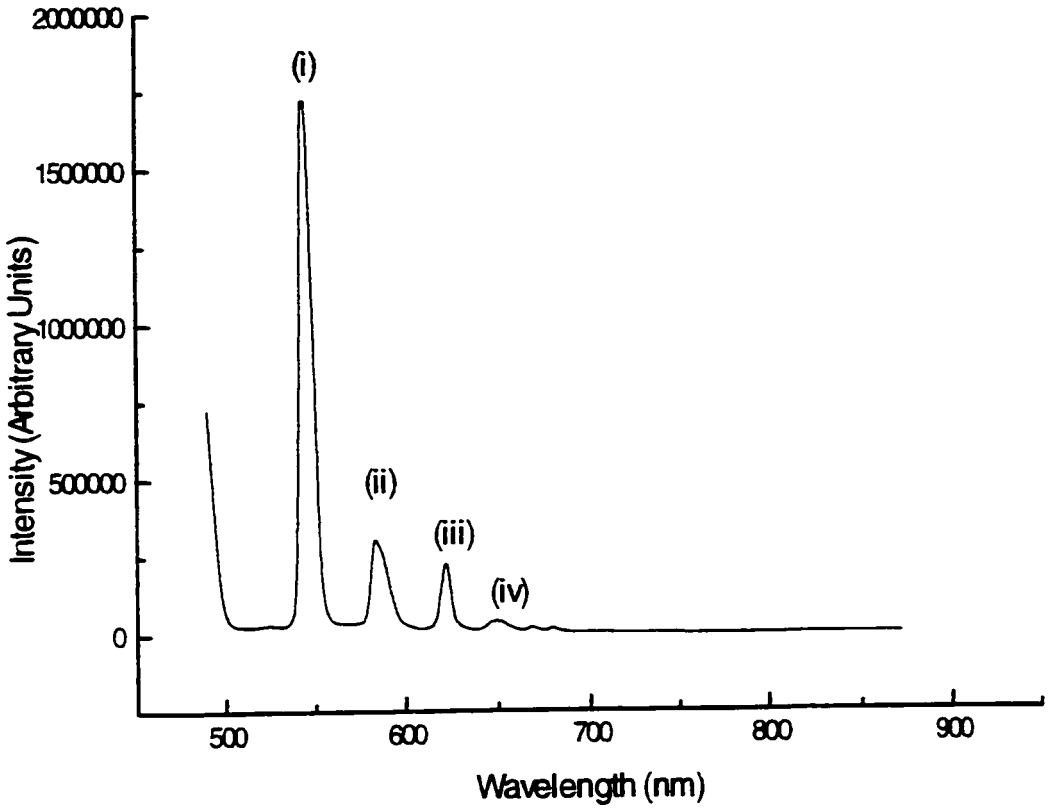

Figure 4.2.2: Emission spectra for the 3 mol% Tb^{3+} doped SiO_2-TiO_2 sample upon 488 nm excitation at 77K;
(i) $^5D_4 \rightarrow {}^7F_5$, (ii) $^5D_4 \rightarrow {}^7F_4$, (iii) $^5D_4 \rightarrow {}^7F_3$ and (iv) $^5D_4 \rightarrow {}^7F_2$.

here there is direct excitation into the $^5D_4$ level thus no induction of non-radiative processes. The following bands were observed at 542, 584, 622, and 648 nm, which can be attributed to the following transitions: $^5D_4 \rightarrow {}^7F_5$, $^5D_4 \rightarrow {}^7F_4$, $^5D_4 \rightarrow {}^7F_3$, and $^5D_4 \rightarrow {}^7F_2$ respectively. All the transitions observed at ambient temperature can also be observed at low temperatures.

The decay time for the 3 mol % Tb^{3+} doped sample at low temperature showed lifetime of 1013 μs.

4.3 Emission Spectroscopy of Co-Doped Sample

Emission of the codoped samples is discussed in this section. In order to study energy transfer between two ions, the SiO_2-TiO_2 sol-gel is codoped with Tb^{3+} and Eu^{3+}. The results in this section will be used to examine the energy transfer process discussed in section 4.6. The samples were prepared by keeping the concentration of the donor ion constant (Tb^{3+}), and varying that of the acceptor ion (Eu^{3+}). The concentration of Tb^{3+} was kept at 3 mol% and the Eu^{3+} varied between 1-5 mol%. Upon 488 nm excitation and at room temperature, the sample containing 3 mol % doped Tb^{3+} and Eu^{3+}, gave rise to bands at 544, 584, 620, 648, and 698 nm as seen in Figure 4.3.1 which can be attributed to the following transitions: $^5D_4 \rightarrow {}^7F_5$, $^5D_4 \rightarrow {}^7F_4$ or $^5D_0 \rightarrow {}^7F_1$, $^5D_4 \rightarrow {}^7F_3$ or $^5D_0 \rightarrow {}^7F_2$, $^5D_4 \rightarrow {}^7F_2$ and $^5D_0 \rightarrow {}^7F_4$ respectively. At 488 nm, there is direct excitation into the $^5D_4$ level of the Tb^{3+} ion as well as excitation into the $^5D_1$ level for the Eu^{3+} ion. The emission spectra for the 3 mol% codoped sample as seen in Figure 4.3.1 shows that there are two

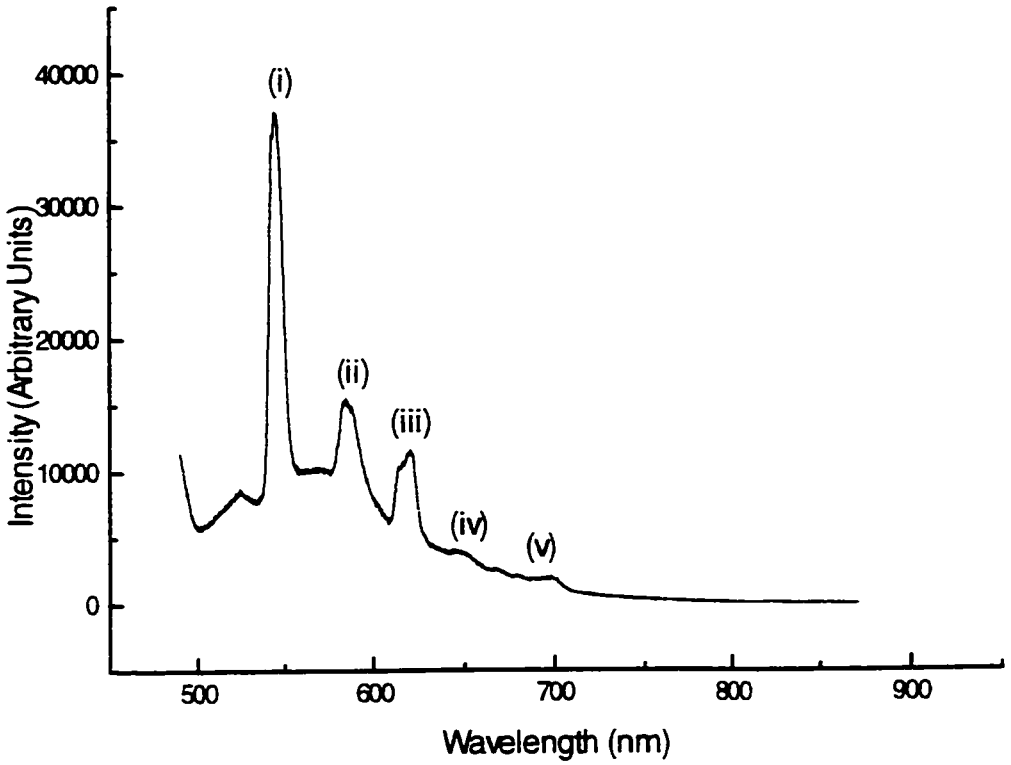

Figure 4.3.1: Emission spectra for the 3 mol% Eu^{3+}-Tb^{3+} doped SiO_2-TiO_2 sample upon 488 nm excitation at room temperature; (i) $^5D_4 \rightarrow {}^7F_5$, (ii) $^5D_4 \rightarrow {}^7F_4/{}^5D_0 \rightarrow {}^7F_1$ (iii) $^5D_4 \rightarrow {}^7F_3/{}^5D_0 \rightarrow {}^7F_2$, (iv) $^5D_4 \rightarrow {}^7F_2$ and (v) $^5D_0 \rightarrow {}^7F_4$.

transitions that can belong to either ion due to the fact they emit at the same energy. By examining the bandwidth, we can clearly see that the bandwidth in the 584 nm region in Figure 4.3.1 is 14.3 nm compared to the same band that appears at 591 nm for Eu^{3+} (11.9 nm) in Figure 4.1.1 and at 584 nm for Tb^{3+} (6.5 nm) in Figure 4.2.1. In section 4.1, the emission spectra for Eu^{3+} at low temperature (Figure 4.1.2) showed that at 77K, no transitions were observed and thus the emission for the 3 mol% codoped sample was examined at low temperature. Figure 4.3.2 shows that there are three transitions that can be observed and are characteristic of Tb^{3+} transitions.

The decay times, at room temperature for the $^5D_0 \rightarrow {}^7F_2$ transition from Eu^{3+} for the codoped samples was monitored for all the samples as shown in Table 4.1.1. In order to understand if any energy transfer was occurring, the decay times for Eu^{3+} within the codoped samples were compared to the decay times for Eu^{3+} samples in the absence of Tb^{3+} ions. It was found that for the codoped sample with 3 mol% doped Tb^{3+} and 3 mol% doped Eu^{3+}, the decay time lengthened from 731 μs (3 mol% Eu^{3+} doped sample) to 853 μs (3 mol% codoped sample). At low temperature as shown in Figure 4.3.2, as expected, no transitions originating from the europium ion were observed due to the fact that at low temperature non-radiative processes do not occur and therefore no emission is observed from the $^5D_0$ level to the lower lying ^7F_J levels. The bands observed were found at 542, 582, and 621 nm in the region of the spectrum which can be attributed to the following transitions: $^5D_4 \rightarrow {}^7F_5$, $^5D_4 \rightarrow {}^7F_4$, and $^5D_4 \rightarrow {}^7F_3$. The transition at $^5D_4 \rightarrow {}^7F_2$ is not observed since the band is very weak and is suppressed by the broad band that originates from the host at low temperature.

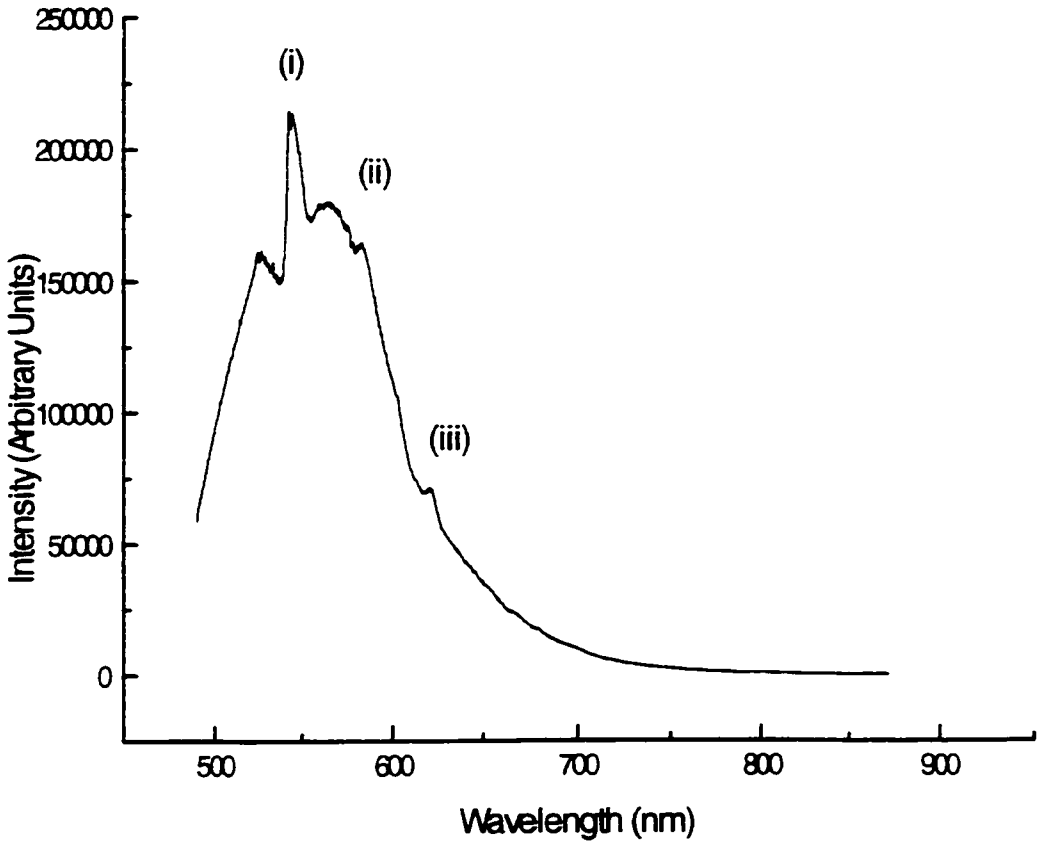

Figure 4.3.2: Emission spectra for the 3 mol% Eu^{3+}-Tb^{3+} doped SiO_2-TiO_2 sample upon 488 nm excitation at 77K;
(i) $^5D_4 \rightarrow {}^7F_5$, (ii) $^5D_4 \rightarrow {}^7F_4$ and (iii) $^5D_4 \rightarrow {}^7F_3$.

4.4 Infrared and Raman Studies

Figures 4.4.1 and 4.4.2 show the infrared spectra for both SiO_2 and TiO_2 powders respectively, in order to better understand what types of stretches to expect in the SiO_2-TiO_2 sol-gel. The SiO_2 and TiO_2 stretches obtained were in good agreement with those found by Fontana et. al [52] and Campostrini and Carturan [53] respectively. The SiO_2 powder showed stretches at approximately 466 cm^{-1}, which can be attributed to the rocking motion of the bridging oxygen atom perpendicular to the Si-O-Si bridging group. At 804 cm^{-1}, where the stretch represents the bending motion of the oxygen atom along the bisector of the Si-O-Si bridging group. The high frequency stretch at approximately 1100 cm^{-1}, due to the asymmetric stretching mode of Si-O-Si groups involving oxygen motion along the Si-Si direction. and the broad stretch at 3436 cm^{-1} due to the water absorbed within the powder. The infrared spectrum for the TiO_2 powder shows a strong stretch between 450 and 700 cm^{-1} typical for titanium samples. It also shows an asymmetric broad absorption centered at approximately 3500 cm^{-1} which can be attributed to the presence of both hydroxyl groups of TiO_2 and adsorbed water. Usually in the presence of water, a stretch at approximately 1630, 1540, and 1430 cm^{-1} can be observed. Due to the fact that the water band is very small at 3500 cm^{-1}, an associated weak band at 1630 cm^{-1} is observed.

Once the infrared stretches were determined for both powders, the infrared spectrum of the host was analyzed as shown in Figure 4.4.3. The SiO_2-TiO_2 host gave rise to the following stretches: 947, 1061, 1454, 1549, 1633, 2396, and 3419 cm^{-1}. These stretches are assigned as follows: the first is attributed to the $Si\text{-}O^-$ stretching originating from Si-O-Ti^{4+}, which means that the titanium ions could be substituting for the silicon ions. The

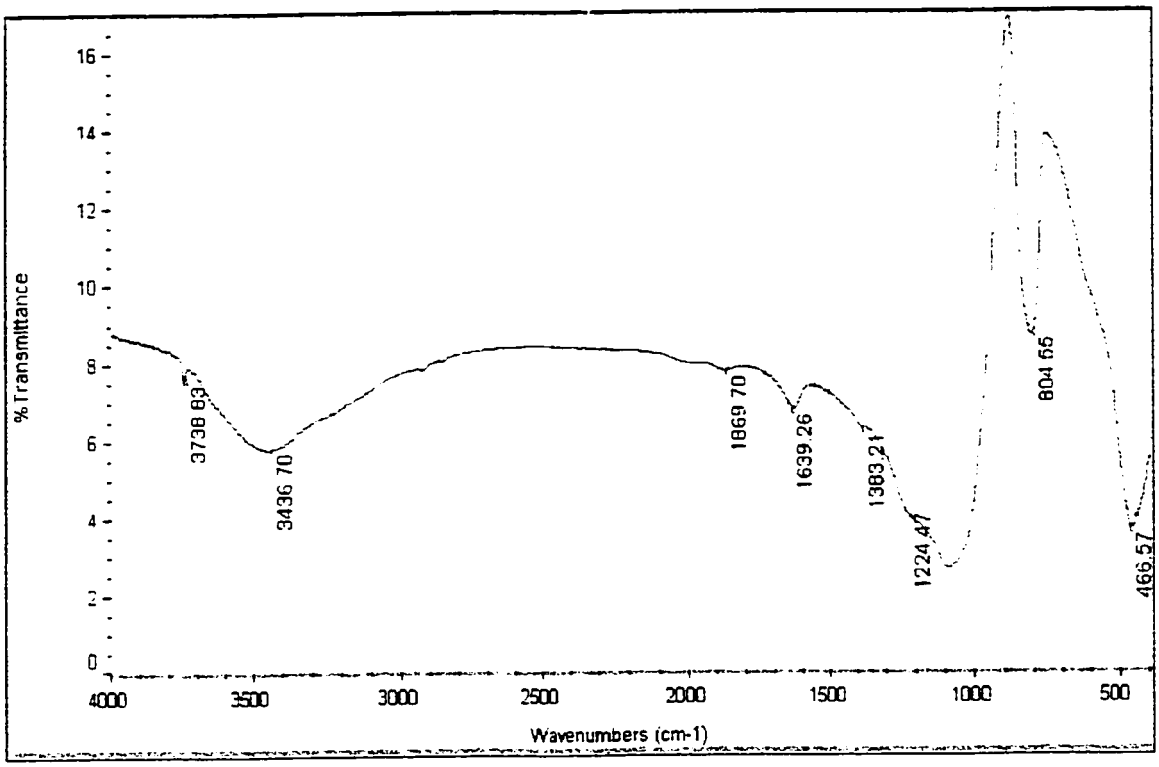

Figure 4.4.1: FTIR for the SiO_2 powder.

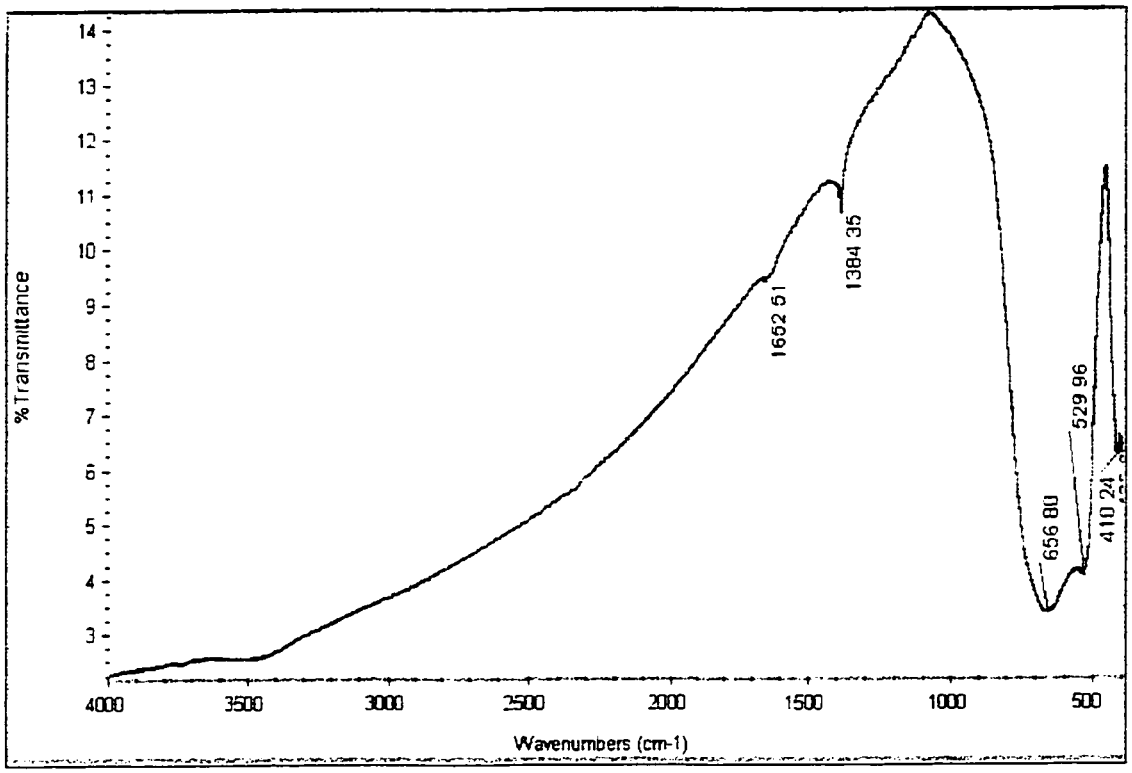

Figure 4.4.2: FTIR for the TiO_2 powder.

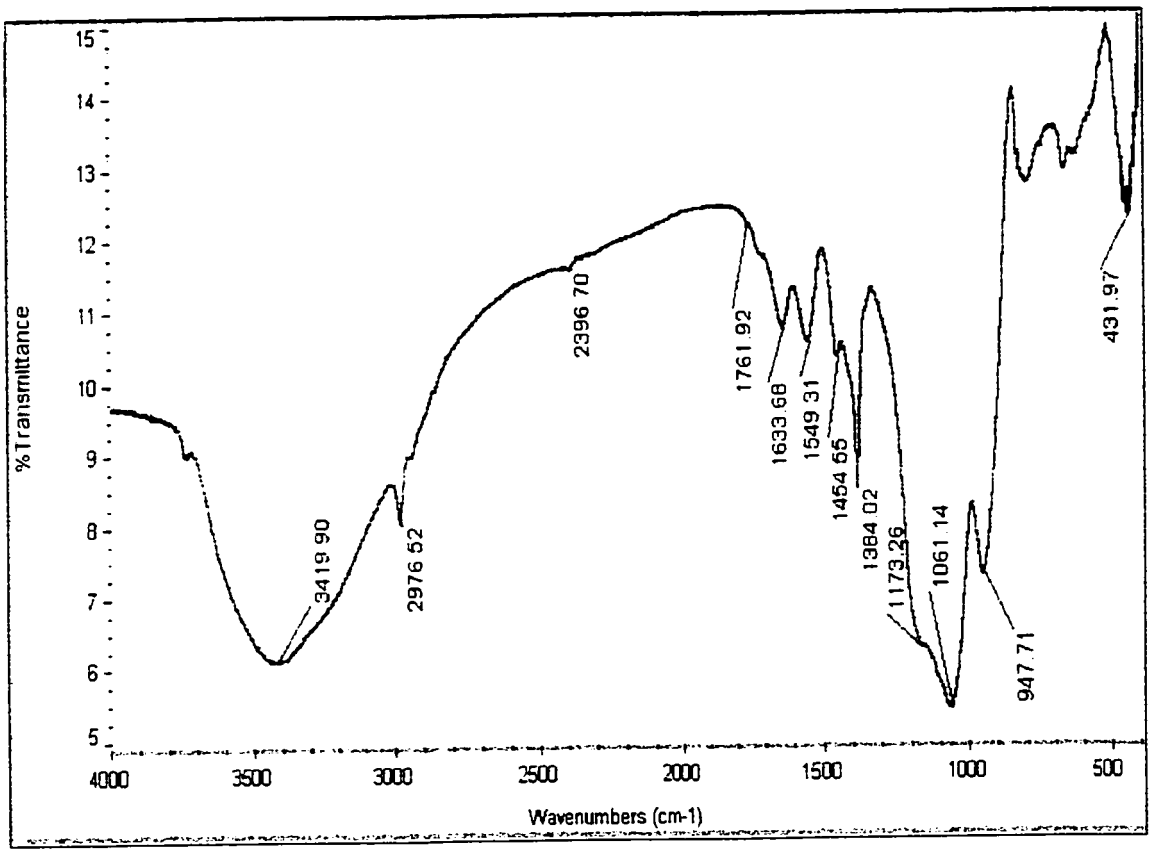

Figure 4.4.3: FTIR for the SiO_2-TiO_2 sol-gel.

second stretch at 1061 cm^{-1} is an Si-O stretch, the third (1454 cm^{-1}) and fourth stretch (1549 cm^{-1}) are small bands due to the bending of Ti-OH groups. The fifth band at 1633 cm^{-1} is due to the relative bending of Si-O and the stretch at 2396 cm^{-1} indicates the presence of an Si-H functional group. The last broad band at 3419 cm^{-1} again can be attributed to the presence of water within the sample. All samples, either doped with Tb^{3+} or Eu^{3+} showed similar results.

Raman studies are used to complement stretches found in the infrared region. Raman transitions are governed by different selection rules from absorption or fluorescence. Thus while in centrosymmetric molecules only ungerade vibrations show up in the infrared absorption spectrum, only gerade vibrations appear in the Raman spectrum. This is the mutual exclusion principle, which states that vibrations active in the infrared spectrum are inactive in the Raman [21]. In this thesis, the sol-gel samples were excited at three different wavelengths (457.98, 501.80, and 514.5 nm) to demonstrate that the Raman scattering is independent of the laser line and therefore at these wavelengths, no emission is observed from Eu^{3+} or Tb^{3+} ions. The intensity of Raman peaks is proportional to the Boltzmann distribution where $I = 1/\lambda^4$.

Raman scattering was observed for the SiO_2 (Figure 4.4.4) and TiO_2 (Figure 4.4.5) powders and for the SiO_2-TiO_2 host (Figure 4.4.6). Raman scattering was also observed for all samples doped with either Tb^{3+} or Eu^{3+}.

According to Nakamoto [54], silicate glass is composed of a network of SiO_4^{4-} tetrahedra connected to each other in such a way that each corner oxygen atom, are shared by a different neighboring tetrahedral unit. There are four modes of vibration, where all four modes are Raman active.

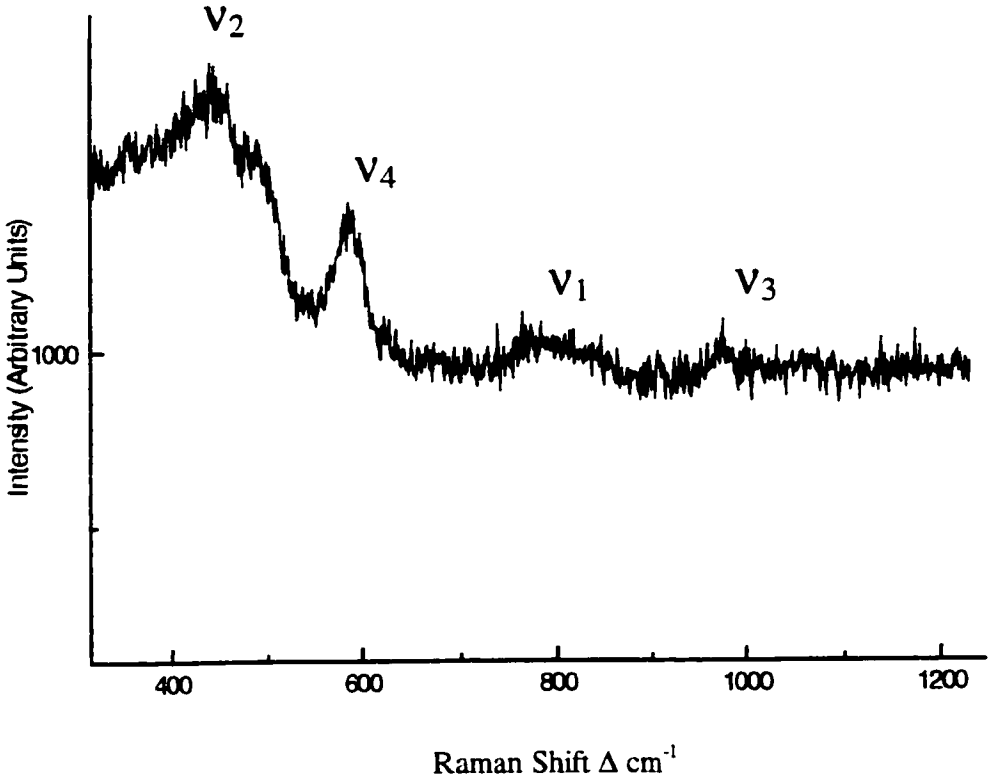

Figure 4.4.4: Raman scattering for the SiO_2 powder upon 457.98 nm excitation at room temperature.

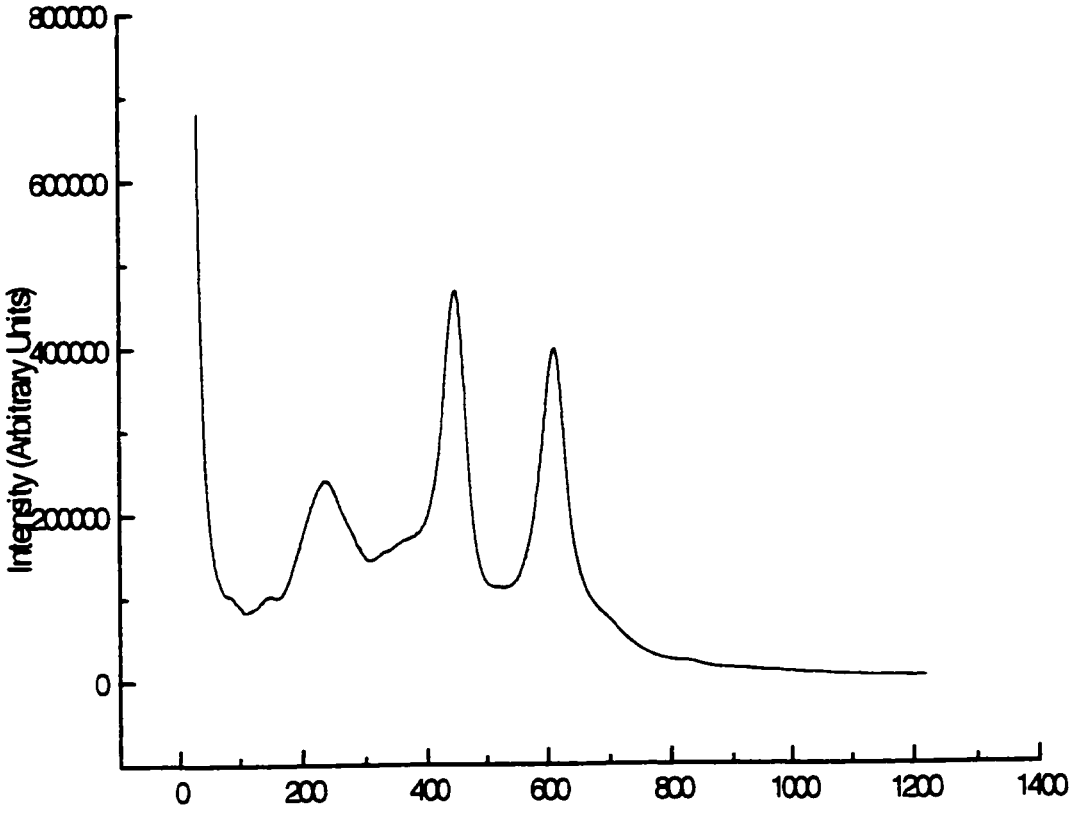

Figure 4.4.5: Raman scattering for the TiO_2 powder upon 514.5 nm excitation at room temperature.

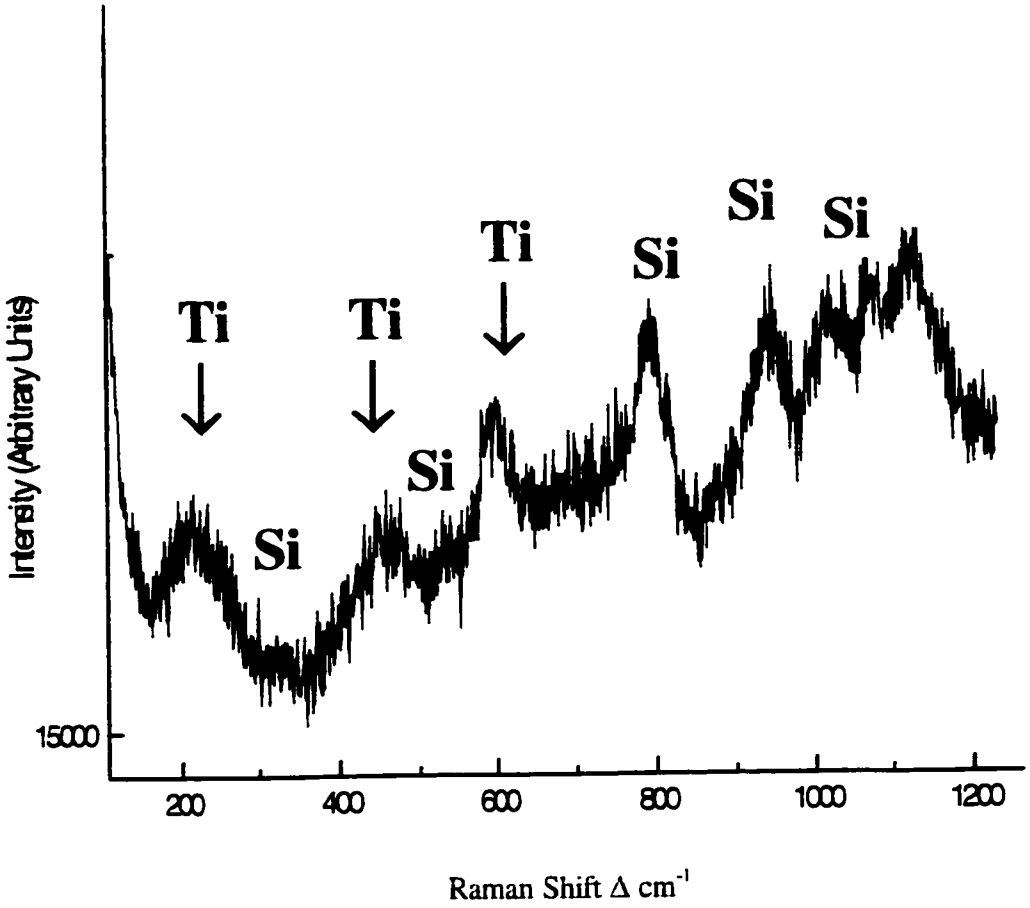

Figure 4.4.6: Raman scattering for the SiO_2-TiO_2 sol-gel upon 457.98 nm excitation at room temperature.

The four vibrations can be found at 340, 527, 819, and 956 cm^{-1} for silicate glass illustrated in Figure 4.4.7.

The SiO_2 powder gave rise to vibrations in good agreement with Fontana [52] and his work on amorphous silica. The modes were found at 428, 612, 810, and 921 cm^{-1}. The TiO_2 powder gave rise to bands at approximately 238, 448, and 605 cm^{-1}. Schraml-Marth et al [55] attributed the band at 238 cm^{-1} as titania lattice modes that become Raman active only after crystallite dimensions are reduced to at least 30 nm, which is consistent with the small size of the titania domains, which in their samples were determined from the shifts in the UV absorption spectra. The band at approximately 440 cm^{-1}, is the most intense and tends to decrease in intensity relative to the band at 605 cm^{-1} as silicon is incorporated within the system. The intensity of the Raman scattering for the TiO_2 powder is higher than that for the SiO_2 powder, but the intensity for each sample is relative.

Once the bands for the SiO_2 (Figure 4.4.4) and TiO_2 (Figure 4.4.5) powders were determined, the Raman scattering for the host material was analyzed. For the SiO_2-TiO_2 host, the following bands were observed: ~ 230, ~ 480, ~ 600, ~ 800, ~ 990, ~ 1100 cm^{-1}, as shown in Figure 4.4.6. These results, were in good agreement with those obtained by Kamitsos and Patsis, [56] and their work on the influence of heat treatment on Raman bands for SiO_2 gels. Their results after heating the gels at 650^{0}C gave the following bands: 495, 606, 815, 981, and 1170 cm^{-1}. The band at 495 cm^{-1} is referred to in the literature as defect band D_1 and has been assigned by Galeener and co-worker [57][58][59] to the symmetric ring breathing mode of four-member rings of SiO_4

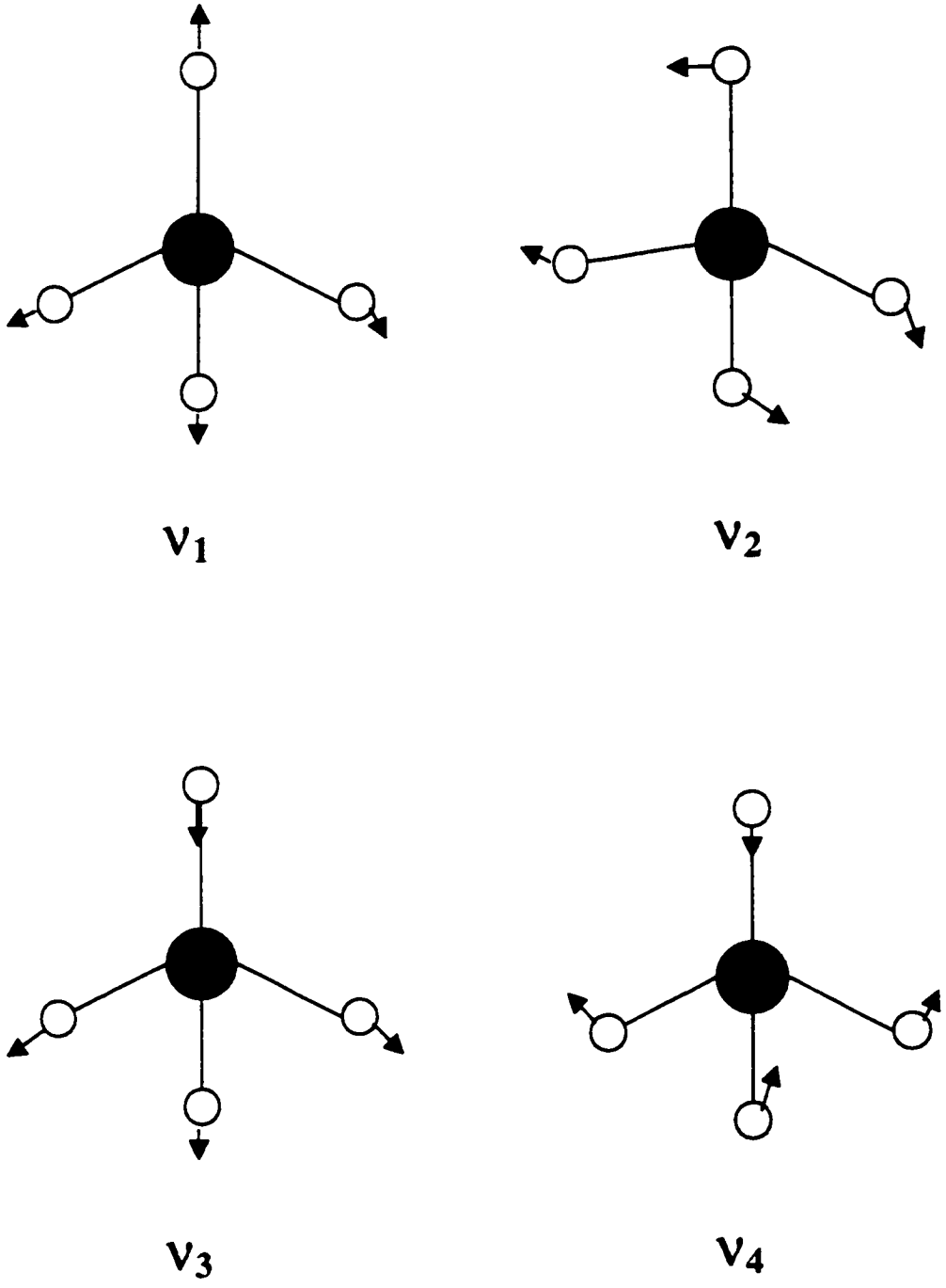

Figure 4.4.7: Four modes of vibration for silicate glass.

tetrahedra. The band at 606 cm^{-1} is known as defect band D_2 and has been assigned to the symmetric ring breathing mode of three-member rings of SiO_4 tetrahedra. The band found at ~ 800 cm^{-1} can be attributed to the deformation mode of the Si-O-Si network as stated by Galeener [57][58][59]. The strong band at ~ 981 cm^{-1} is typical of the Si-O stretching vibration of silanol groups and the band at 1170 cm^{-1} although small in the literature results, shows a high intensity in our host sample. This band usually increases in intensity the higher the heat treatment. Since the samples in this thesis were not heated more than 200°C, this band is very weak and is most probably due to the asymmetric stretching of Si-O-Si linkages.

The remaining bands found in the host (SiO_2-TiO_2) originate from the titanium dioxide present in the sample. The bands are found at ~ 230, 480, and 600 cm^{-1} where the band at 230 cm^{-1} is attributed to titania lattice modes as previously mentioned.

4.5 D_2O Substitution

Glasses and sol-gels cured at room temperature or at temperatures below 150°C are expected to contain some residual amounts of water and alcohol. These hydroxyl and alcohol groups might surround the rare earth ion in question thereby providing a way to induce non-radiative relaxations in rare-earth doped sol-gel materials. A shorter decay time is an indication for this high non-radiative decay rate arising from an increase in hydroxyl groups that can be found in the immediate vicinity of the Eu^{3+} or Tb^{3+} ion. The substitution of H_2O with D_2O provides information of the "real" lifetime of an energy level by partial elimination of the non-radiative component. D_2O is used as a substitution for H_2O since the O-D has a smaller vibrational energy as compared to the vibrational energy

for O-H and thus more quanta is required to allow non-radiative decay of the Eu^{3+} ion to its ground state. As a result, non-radiative decay is less probable and its rate decreases, which subsequently intensifies the fluorescent intensity and increases the radiative decay time [60]. In this thesis, an increase in lifetimes has been observed for all samples as well as a decrease in intensity of the band usually found at approximately 525 nm attributed the OH vibrations.

Figure 4.5.1 shows the spectrum of the 3 mol% doped Eu^{3+} sample with H_2O as a hydrolyzing agent compared with the same sample with D_2O substitution. It can clearly be seen that the region around 525 nm is less intense for the D_2O substituted sample. The decay times for all samples that were hydrolyzed using H_2O and D_2O are summarized in Table 4.5.1.

4.6 Energy Transfer

Rare earth ions are particularly suitable for the study of energy transfer since the absorption and emission due to the f-electrons is sharp and the associated oscillator strengths are weak. The energy transfer process was examined for the sample that was doped with 3 mol% Tb^{3+} and 3 mol% Eu^{3+} due to the fact that the lifetimes for the $^5D_0$ level of the Eu^{3+} ion lengthened in the presence of the donor ion from 0.73 ms to 0.85 ms as shown in Table 4.1.1. The lengthening of the lifetime is due to the fact that some of the energy from Tb^{3+} is transferred to the Eu^{3+} ion. The energy gap between the $^5D_4$ and $^5D_0$ levels of the Tb^{3+} and Eu^{3+} ion respectively is approximately 3500 cm^{-1}, as demonstrated in the energy level diagram in Figure 1.3.1. The cutoff phonon energy for the SiO_2-TiO_2 host as determined from Raman studies was found to be approximately 1100 cm^{-1}.

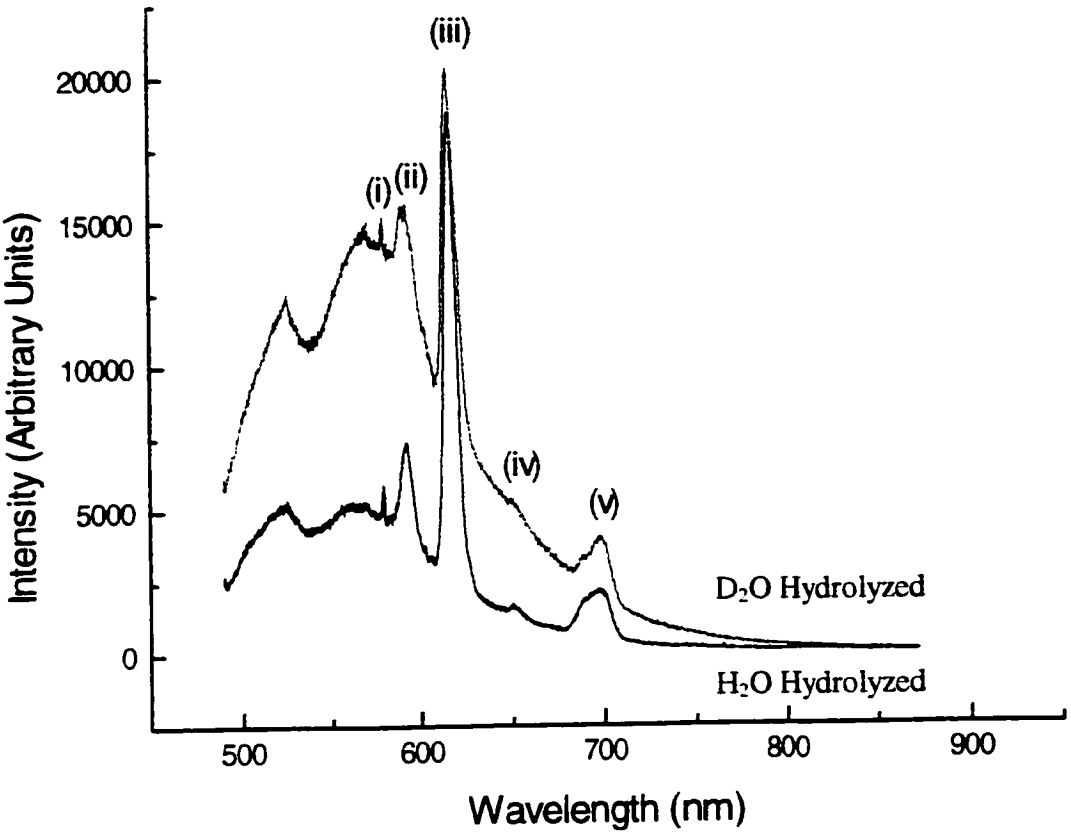

Figure 4.5.1 Emission spectra for the 3 mol% Eu^{3+} doped sample hydrolyzed with D_2O and H_2O upon 488 nm excitation and room temperature.

Sample	H_2O – Acid Catalyzed Lifetime (μs)	D_2O – Acid Catalyzed Lifetime (μs)
1 mol% Eu	1127	------
2 mol% Eu	1114	1175
3 mol% Eu	731	1206
4 mol% Eu	730, 390	1304
5 mol% Eu	802	1264
1 mol% Tb	1012	------
2 mol% Tb	1027	1240
3 mol% Tb	1001	1213
4 mol% Tb	1167	1304
5 mol% Tb	956	1190

Table 4.5.1 : Lifetimes for Eu^{3+} and Tb^{3+} doped SiO_2-TiO_2 samples hydrolyzed with H_2O and D_2O upon 488 nm excitation and room temperature.

The cutoff phonon energy was determined to be 1100 cm^{-1} as stated in the literature since this is the highest phonon vibration in the SiO_2-TiO_2 host. The energy transfer process is believed to proceed via a non-resonant energy transfer based on the results obtained from the emission spectra, decay times and phonon energies associated with the sol-gel host. Non-resonant energy transfer involves the mismatch of energy between two ions where this mismatch or energy gap is compensated by the transfer of one or more phonons from the donor ion to the acceptor ion thus called a phonon-assisted energy transfer process. At room temperature and an excitation wavelength of 488 nm, the $^5D_4$ level of the Tb^{3+} ion is directly excited with subsequent emission down to the lower lying ^7F_J states. A portion of its energy is then transferred to the $^5D_1$ level belonging to the Eu^{3+} ion which non-radiatively decays down to the $^5D_0$ level and emission is therefore observed from the $^5D_0$ level to the lower lying ^7F_J levels. The energy transferred from donor to acceptor ion proceeds through the assistance of three phonons. This is due to the fact that the energy gap between the $^5D_4$ level of the Tb^{3+} ion and the $^5D_0$ level for the Eu^{3+} ions is approximately 3500 cm^{-1} and the cutoff phonon energy for the SiO_2-TiO_2 host is approximately 1100 cm^{-1}, therefore resulting in approximately three phonons. The energy transfer process is illustrated in Figure 4.6.1.

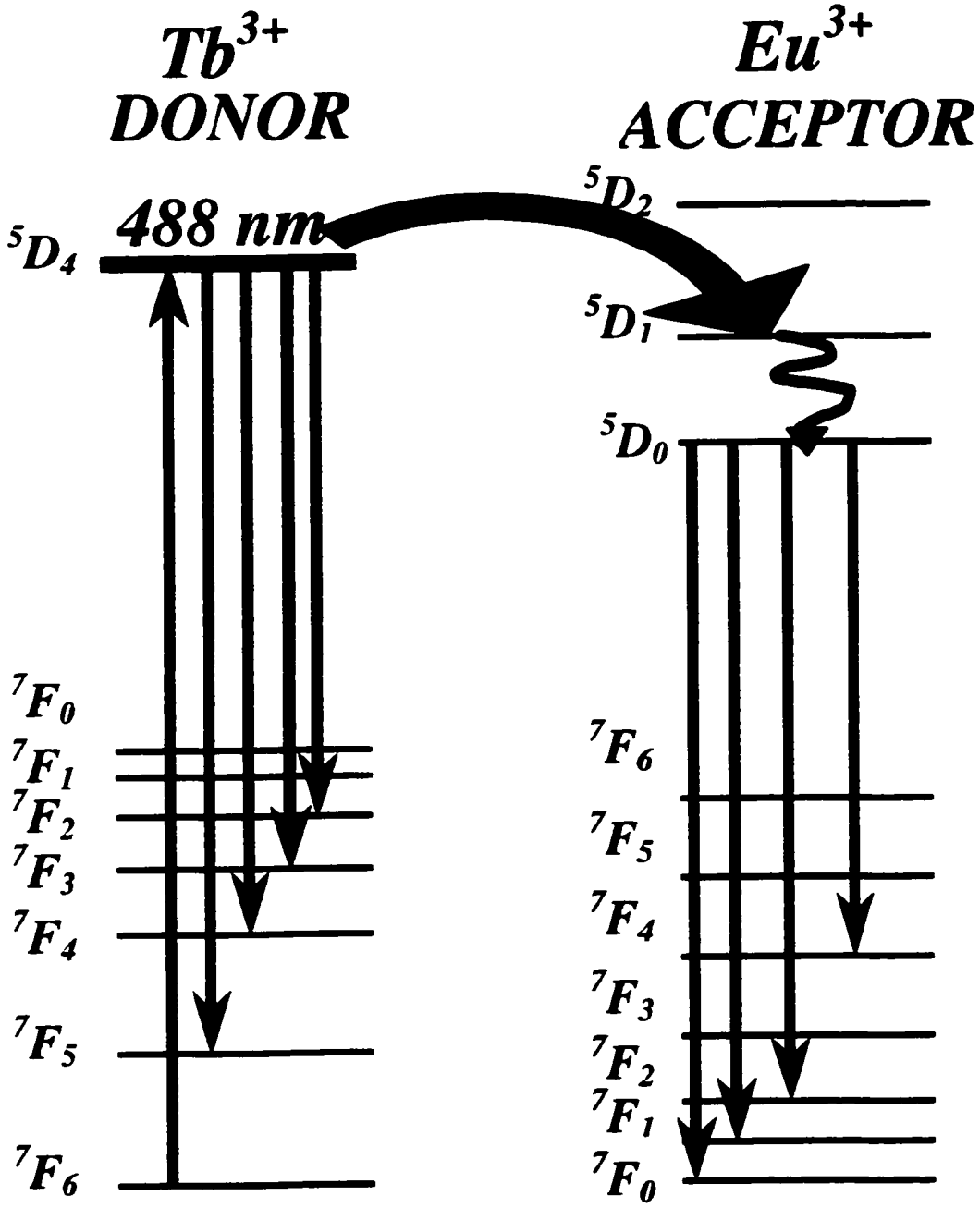

Figure 4.6.1: Phonon-Assisted energy transfer mechanism between Tb^{3+} and Eu^{3+}.

4.7 Waveguides

Waveguides were obtained through the dip coating technique as described in Chapter 3 and were coated on glass slides. Waveguide studies were performed for a 5 mol% Eu^{3+} doped sample at room temperature and an excitation wavelength of 488 nm. Bands observed were found at 579, 592, 615, 650, and 697 nm which can be attributed to the following transitions: $^5D_0 \rightarrow {}^7F_0$, $^5D_0 \rightarrow {}^7F_1$, $^5D_0 \rightarrow {}^7F_2$, $^5D_0 \rightarrow {}^7F_3$, and $^5D_0 \rightarrow {}^7F_4$ respectively. The spectra obtained for the waveguide shows better resolution of peaks and a reduction in the OH vibration as compared to that of the 5 mol% Eu^{3+} sol-gel as demonstrated in Figure 4.7.1.

The waveguide propagation along the glass slide was captured using a digital camera as shown in Figure 4.7.2. In order to obtain these photographs, an excitation wavelength of 514.5 nm was used instead of 488 nm due to the fact that there is direct excitation into the $^5D_0$ level and therefore a more intense signal. Although an excitation wavelength of 514.5 nm was used it should be noted that the waveguide propagation can be seen at both wavelengths with the naked eye.

Figure 4.7.3 demonstrates the angle at which the beam is reflected from the film-cover interface. According to Figure 4.7.3, there is no evidence of the Goos-Hanchen shift (with the naked eye) proving that there is complete reflection from the film-cover interface as well as for the substrate-

likely at less than 1μm and therefore further examination must be done in the future using m-line spectroscopy or by the incorporation of a phosphor that can capture the scattered light.

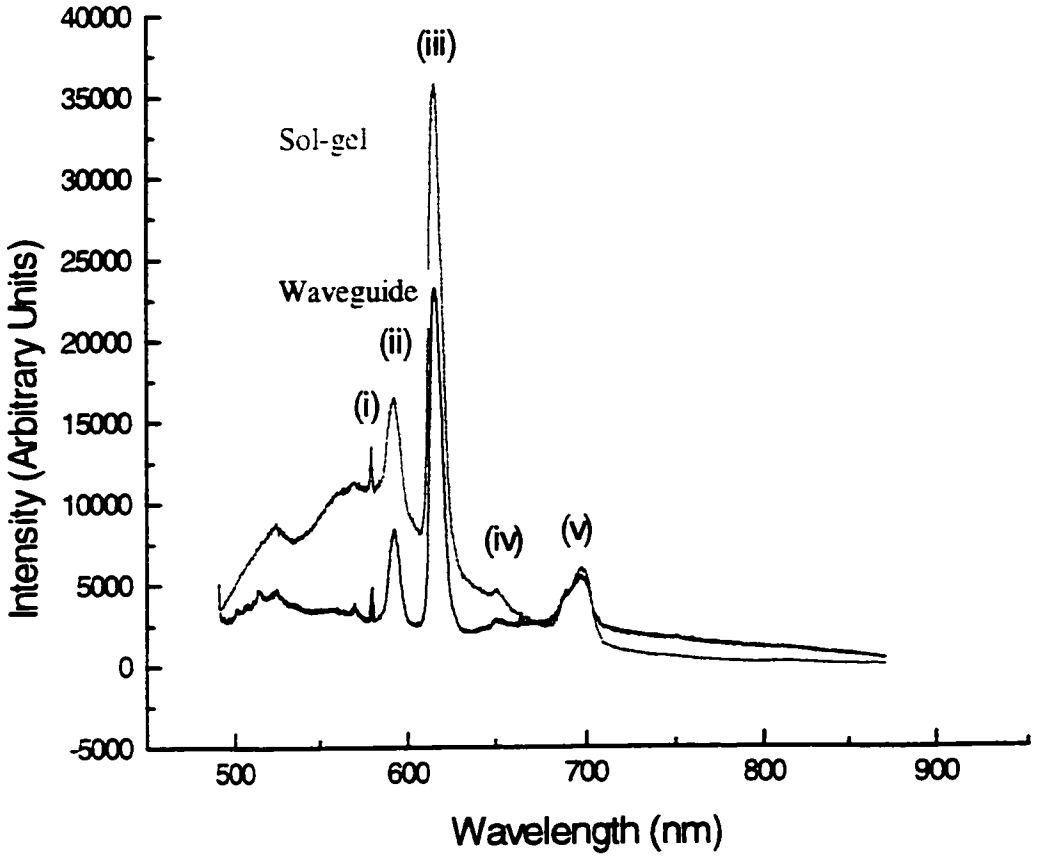

Figure 4.7.1: Emission spectra for the 5 mol% Eu^{3+} doped SiO_2-TiO_2 sol-gel and waveguide upon 488 nm excitation at room temperature; (i) $^5D_0 \rightarrow {}^7F_0$, (ii) $^5D_0 \rightarrow {}^7F_1$ (iii) $^5D_0 \rightarrow {}^7F_2$, (iv) $^5D_0 \rightarrow {}^7F_3$ and (v) $^5D_0 \rightarrow {}^7F_4$.

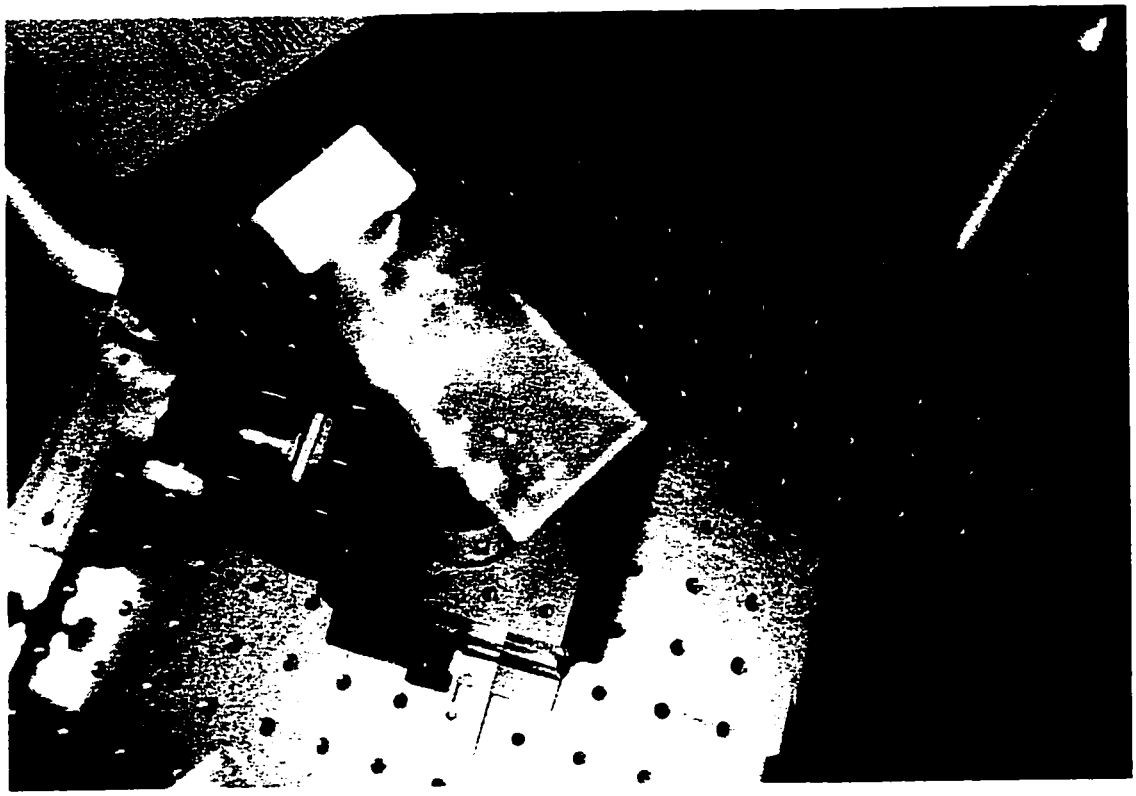

Figure 4.7.2 : Waveguide propagation for the 5 mol% Eu^{3+} doped SiO_2-TiO_2 waveguide upon 514.5 nm excitation and room temperature.

Figure 4.7.3 : Waveguide propagation for the 5 mol% Eu^{3+} doped SiO_2-TiO_2 waveguide upon 514.5 nm excitation and room temperature. The film-cover interface is shown above.

4.8 SiO_2-TiO_2 Network

Knowing what types of stretches are observed for the infrared and Raman experiments, the structure of the network can be deduced. Silica's presence delays the crystallization of titania to higher temperatures. These effects have been related to silica's ability to impede titania's normal sintering processes through formation of Ti-O-Si "hetero-linkages". According to the infrared spectrum of the host material, the stretch found at approximately 947 cm^{-1} originates from an Si-O-Ti linkage. This means that the titanium that is entering the system is replacing the silicon atoms in the silicon tetrahedral network. Pratt [61] suggests that titania is sparsely soluble in silicate rich melts and this has been used throughout history as an opacifier in glasses, glazes and enamels of all types. Pratt also states that when titania is added to an SiO_2 rich parent glass, to the extent that Ti can be dissolved by the given composition, TiO_2 assumes a spot in the Si-O glassy network effectively replacing the Si-O. This would mean that Ti would weaken the silicate network somewhat. This has been seen in the manufacture of glasses a diverse as fused quartz and vitreous enamel where Ti lowers the viscosity in the former and adds chemical durability to the latter. Stretches at 1549 and 2396 cm^{-1} suggest that there are Ti-OH groups and Si-H functional groups respectively within the structure. Knowing that the titania successfully substitutes for the silica, the next step is to study how the rare earth ions are incorporated within the network. It is obvious that Eu^{3+} or Tb^{3+} ions must coordinate to an oxygen atom. The silicon and titanium ions have a coordination of four and thus have four oxygen ligands surrounding them. This means that the Eu^{3+} or Tb^{3+} will coordinate to one of the oxygen ligands from either the silicon for titanium. A more detailed infrared study would need to be done in order to examine the Eu-O and Tb-O

stretches. Figure 4.8.1 gives a schematic representation of the structure of the network.

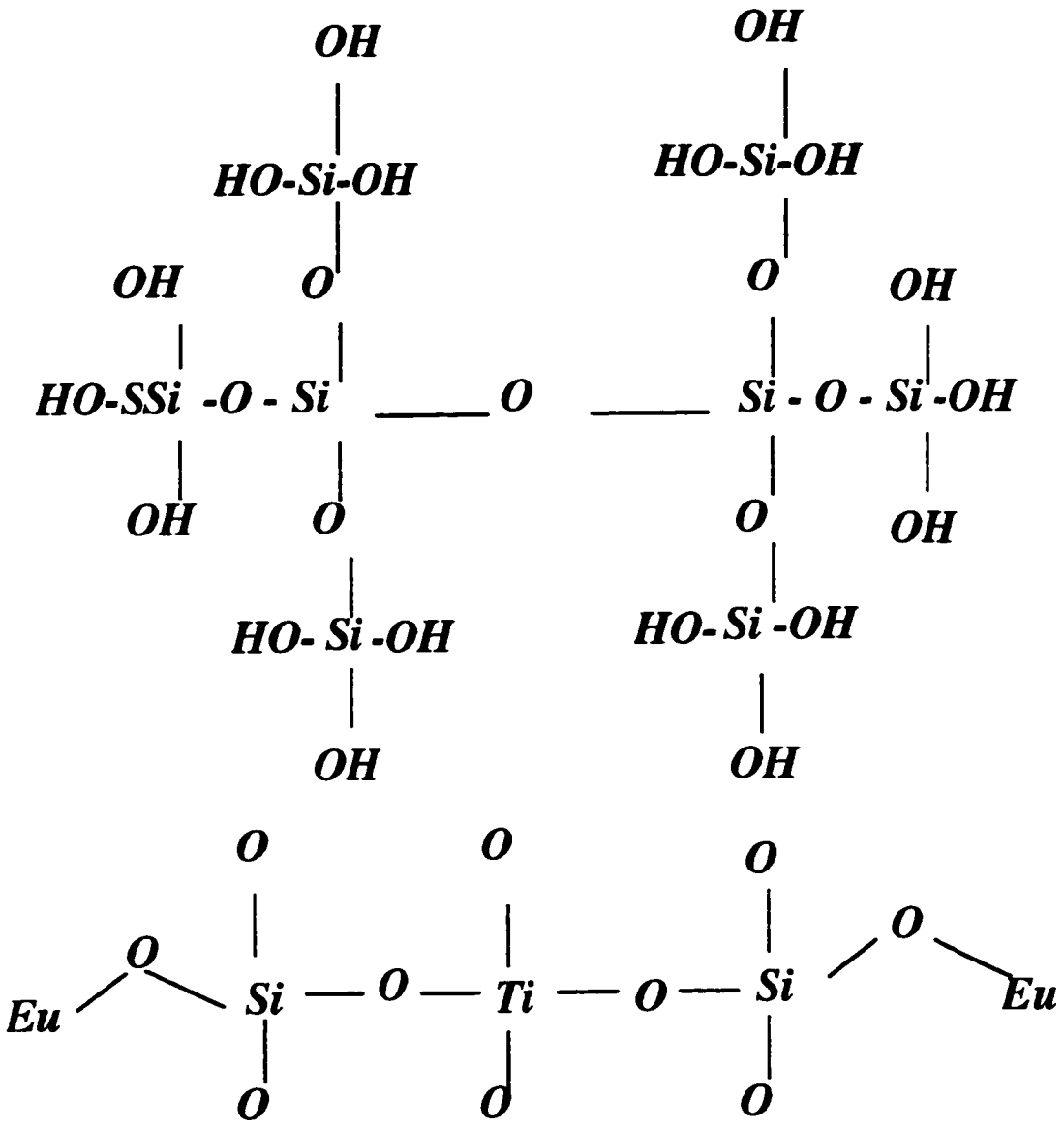

Figure 4.8.1: Probable structure of the SiO_2-TiO_2 network doped with Eu^{3+} ions. First structure shows the SiO_2 network.

4.9 REFERENCES

[1] M. Ebelman, Ann. Chimie Phys., 16, 129 (1846).

[2] T. Graham, J. Chem. Soc., 17, 318 (1864).

[3] W.Z. Ostwald, Phys. Chem., 27, 365 (1897).

[4] L. Rayleigh, Philos. Mag., 38, 738 (1919).

[5] L. Hench, J.K. West, Chem. Rev., 90, 33 (1990).

[6] D.M, Roy, R. Roy, Am. Mineral, 39, 357 (1954).

[7] R.K. Iler, The Chemistry of Silica. Wiley, New York, 1955.

[8] W. Stoeber, A. Fink, E.J. Bohn, Colloid Interface Sci., 26, 62 (1968).

[9] H. Schroder, Phys. Thin Film, 87 (1969).

[10] J.C. Brinker, ACS. Advances In Chemistry Series, 234, 361 (1994).

[11] R.W. Jones, Fundamental principles of sol-gel technology. Institute of Metals, 1989.

[12] T.H.C. Nguyen, "CMZP and Mg-doped Al_2TiO_5 Thin Film Coatings for High Temperature Corrosion Protection of Si_3N_4 Heat Exchanges", M.Sc. Thesis, Virginia Polytechnic Institute and State University, Blacksburg,Virginia, 1998.

[13] A.B. Peri, J. Phys. Chem., 70, 2937 (1966).

[14] C. Chappe, K. Steinbuch, Die informierte Gesellschaft, 60-66, Sluttgart, 1966.

[15] M.J. Howes, D.V. Morgan, Optical Fiber Communication. John Wiley and Sons, New York, 1980.

[16] A.G. Bell, "Selenium and the photophone", The Electrician", 214, 1880.

[17] D.B. Anderson, Optical and Electro-optical Information Processing. MII Press, 1965.

[18] W.O Grant, Understanding Lightwave Transmission. Technology publications, 1988.

[19] P.K. Tien, Appl. Opt., 10 (11), 2395 (1971).

[20] H. Kogelnik, Guided-Wave Optoelectronics. Springer-Verlag, Berlin, 1988.

[21] D.L. Andrews, Lasers in Chemistry 3rd Edition. Springer-Verlag, Berlin, 1997.

[22] N. Kaltsoyannis, P. Scott, The f Elements. Oxford University Press, Oxford, 1999.

[23] H. J. Zhang, L.S. Fu, S.B Wang, Q.G Wang, K.Y. Yang, J.Z. Ni, Mater. Lett. 38(4), 260 (1999).

[24] J. Singh, Excitation energy transfer process in condensed matter. Plenum Press, New York, 1995.

[25] T. Forster, Ann. Phys., 2, 55 (1948).

[26] D.L. Dexter, J. Chem. Phys., 21, 836 (1953).

[27] M. Inokuti, F. Hirayama, J. Chem. Phys., 43, 1978 (1965).

[28] T. P.J. Botden, Philips Res. Rep., 7, 197 (1952).

[29] D.L. Dexter, J.H. Schulman, J. Chem. Phys., 22, 1063 (1954).

[30] R.A. Hewes, J.F. Sarver, Phys. Rev., 182, 427 (1969).

[31] L.F. Johnson, H.J. Guggenheim, Appl. Phys. Lett., 19, 44 (1971).

[32] X.J. Wang, L. Matthews, R. Lowell, E.T. Knobbe, Materials Res. Soc. Symposia Proceedings, 328, 745 (1994).

[33] S. Murakami, M. Herren, D. Rau, T. Sakurai, M. Morita, J. Lumin., 83 & 84, 215-219 (1999).

[34] L.S. Fu, H.J Zhang, S.B Wang, Q.G Meng, K.Y Yang, J.Z Ni, Chin. J. Chem., 17(2), 132 (1999).

[35] R.C. Ropp, J. Opt. Soc. of Am., 57(2), 213 (1967).

[36] M. Bettinelli, C.D. Flint, J. Phys. Condens. Matter 2, 8417 (1990).

[37] M.J. Lochhead, K.L. Bray, J. Non-Cryst. Solids., 170, 143 (1994).

[38] E.M. Yeatman, M.M. Ahmad, O. McCarthy, A. Vannucci, P. Gastaldo, D. Barbier. D. Mongardien, C. Moronvalle, Opt. Comm. 164 (1), 19 (1999).

[39] Merck Index 12th Ed. Merck Research Laboratories, New Jersey 1996.

[40] C.J. Brinker, R. Sehgal, S.L. Hietala, R. Deshpande, D.M. Smith, D. Loy, C.S. Ashley, J. Membrane Sci. 94,85 (1994).

[41] Y. Takahashi, Y. Wada, J. Electrochem. Soc., 137, 267 (1990).

[42] J. Livage, M. Henry, C. Sanchez, Sol-gel chemistry of transition metal oxides, Prog. Solid State Chem., 18, 259 (1988).

[43] J.L Hall, W.E. Dean, E.A. Pacofsky, J. Am. Chem. Soc., 82, 3303 (1960).

[44] G.W. Scherer, J. Non-Cryst. Solids, 147 & 148, 363 (1992).

[45] C.J Brinker and G.W. Scherer, Sol-gel Science. Academic Press, San Diego, 1990.

[46] B., Henderson, G.F. Imbusch, Optical Spectroscopy of Inorganic Solids. 1985.

[47] T. Forster, Disc. Faraday Soc., 27, 7 (1959).

[48] E. Nakazawa, S. Shionoya, J. Chem. Phys. 43, 1978-1989 (1965).

[49] P.K. Gallagher, J. Chem. Phys., 41, 10 (1964).

[50] C. Brecher, L.A. Riseberg, J. Non-Cryst. Solids, 40, 469 (1980).

[51] C. Armellini, L. Del Longo, M. Ferrari, M. Montagna, G. Pucker, P. Sagoo, J. Sol-Gel Sci. 13, 599-603 (1998).

[52] A. Fontana, E. Moser, F. Rossi, R. Campostrini, G. Carturan, J. Non-Cryst. Solids, 212, 292 (1997).

[53] R. Campostrini, G. Carturan, L. Palmisano, M. Schiavello, A. Sclafani, Materials Chem. and Phys., 38, 277 (1994).

[54] K. Nakamoto, Infrared and Raman Spectra of Inorganic and Coordination Compounds. 4th Ed. Wiley, New York, 1986.

[55] M. Schraml-Marth, K.L. Walther, A. Wokaun, B.E. Handy, A. Baiker, J. Non-Cryst. Solids, 143, 93 (1992).

[56] E.I. Kamitsos, A.P. Patsis, Phys. Rev. B, 48 (17), 12499 (1993).

[57] F.L. Galeener, Solid State Commun. 44, 1037 (1982).

[58] F.L Galeener, A.E. Geissberger, Phys. Rev. B. 27, 6199 (1983).

[59] F.L. Galeener, J. Non-Cryst Solids, 49, 53 (1982); 71, 373 (1985).

[60] K. Devlin, B. O'Kelly, Z.R. Tang, C. McDonagh, J.F. McGilp, J. Non-Cryst. Solids, 135, 8 (1991).

[61] K. Platt, Titania in Glazes . The Ceramics Web, 1994.

[62] R. Le Van Mao, S.T. Le, D. Ohayon, F. Caillibot, L. Gelebart, and G. Denes, Zeolites 19, 270-278, 1997.

Chapter 5

5.1 Conclusion

The energy levels at room temperature for Eu^{3+} and Tb^{3+} doped in an SiO_2-TiO_2 host at doping concentrations of 1 to 5 mol% were established for both H_2O and D_2O hydrolyzed systems. The transitions observed for Eu^{3+} samples were as follows: $^5D_0 \rightarrow {}^7F_0$, $^5D_0 \rightarrow {}^7F_1$, $^5D_0 \rightarrow {}^7F_2$, $^5D_0 \rightarrow {}^7F_3$, and $^5D_0 \rightarrow {}^7F_4$. Transitions belonging to Tb^{3+} were $^5D_4 \rightarrow {}^7F_5$, $^5D_4 \rightarrow {}^7F_4$, $^5D_4 \rightarrow {}^7F_3$, and $^5D_4 \rightarrow {}^7F_2$. These transitions were observed for both H_2O and D_2O hydrolyzed samples. Low temperature emission studies for Eu^{3+} at an excitation wavelength of 488 nm gave rise to one large broad band as expected due to the fact that the non-radiative component is eliminated at low temperatures and therefore no emission from the $^5D_0$ level is observed. On the other hand low temperature emission for Tb^{3+} doped samples at an excitation wavelength of 488 nm gave rise to the same transitions as those observed for Tb^{3+} doped samples at room temperature due to the fact that there is direct excitation of the $^5D_4$ level at this wavelength. A comparison of lifetimes for samples hydrolyzed with H_2O and D_2O for both rare earth doped samples showed an increase in lifetimes when D_2O was present. This suggests that due to the smaller vibrational quanta for D-O as compared to O-H, there is a smaller non-radiative decay rate and thus an accompanying increase in lifetime. Codoped samples at room temperature and excitation wavelength of 488 nm where the concentration of Tb^{3+} was kept constant at 3 mol% and that of Eu^{3+} varied between 1-5 mol% were examined. The emission spectra gave rise to transitions that are characteristic of Tb^{3+} with the possibility of two transitions that are characteristic of Eu^{3+}. This was observed due to the fact that at an excitation wavelength

of 488 nm and room temperature, Tb^{3+} and Eu^{3+} samples have transitions that emit at the same energy. Low temperature studies of the codoped samples showed transitions that are characteristic of Tb^{3+} only. The transitions observed were, $^5D_4 \rightarrow {}^7F_5$, $^5D_4 \rightarrow {}^7F_4$, and $^5D_4 \rightarrow {}^7F_3$. From the emission observed for the codoped sample, it was shown that at 3 mol% Tb^{3+} and 3 mol% Eu^{3+} the lifetime of the $^5D_0 \rightarrow {}^7F_2$ transition lengthened in time suggesting energy transfer processes. Lifetime studies, coupled with Raman scattering of the host concluded that there is a phonon-assisted energy transfer taking place where the Tb^{3+} donor ion transfers a portion of its energy to Eu^{3+} acceptor ion. It was determined that it takes three phonons to cover the energy gap between the $^5D_4$ level of the Tb^{3+} ion and the $^5D_0$ level for the Eu^{3+} ion.

Waveguide studies confirmed that there is evidence of light propagation in a 5 mol% doped Eu^{3+} sample. The observed transitions for the waveguide were as follows: $^5D_0 \rightarrow {}^7F_0$, $^5D_0 \rightarrow {}^7F_1$, $^5D_0 \rightarrow {}^7F_2$, $^5D_0 \rightarrow {}^7F_3$, and $^5D_0 \rightarrow {}^7F_4$ similar to that observed for the 5 mol% doped Eu^{3+} sol-gel. Further investigation shows that there is no shift into the film-cover interface, suggesting a good reflection from the film-cover and substrate-film interfaces.

Infrared studies showed that stretches found for SiO_2 and TiO_2 powders were similar to those found for the SiO_2-TiO_2 host. The stretches observed were as follows: 947, 1061, 1454, 549, 1633, 2396, and 3419 cm^{-1}. These stretches are assigned as follows: the first is attributed to the $Si\text{-}O^-$ stretch that originates from an $Si\text{-}O\text{-}Ti^{4+}$ linkage, and the second stretch is assigned as an Si-O group. The third and fourth stretch are weak and are due to the bending of Ti-OH groups. The fifth stretch is due to the relative bending of the Si-O group, and the sixth stretch indicates the presence of an Si-H functional group. The band

at 3419 cm^{-1} is due to the presence of water within the sample. The Raman scattering for the SiO_2-TiO_2 host gave the following bands: 230, 480, 600, 800, 990, and 1100 cm^{-1}. These bands are in good agreement with those found in the literature and these results were compared to the Raman scattering obtained for the SiO_2 and TiO_2 powders.

The IR and Raman studies provided information necessary to investigate the overall structure of the network. For instance, it is clear that the rare earth ions are coordinated to oxygen atoms and that the titanium atoms substitute for the silicon atoms. There is also evidence that there are some titanium atoms that are bound to OH groups as well as silicon atoms bound to hydrogen atoms.

5.2 Future Works

The results obtained in this thesis can lead to further research in the field of sol-gel and waveguide technology. The preparation technique can be altered to include base catalysis instead of acid catalysis and thus a study on the surface area can be done to compare the size of the pores. The size of the pores is important to determine what drying method is appropriate to yield homogeneous, crack free sol-gels. In the area of energy transfer, a temperature study should be done in order to determine at what temperature energy transfer becomes less efficient. Low temperature studies of sol-gels hydrolyzed with D_2O should also be done in order to investigate the probability of reducing the non-radiative component found in europium based systems.

In order to fully understand the substitution of titanium within the network, more extensive FTIR studies must be done. FTIR spectroscopy can give information concerning the amorphous substitution of titanium for silicon by analyzing the strong asymmetric stretch found at 1100 cm^{-1}. Studies by Mao et al [62] on zeolites demonstrates that there is a shift of this asymmetric stretch between the parent zeolite and the desilicated zeolite, since desilication results in an increase in the number of framework Al-O-Si bonds. In other words, as titanium is incorporated within the SiO_2 network, presence of a shift in the asymmetric stretch would confirm a Ti-O-Si substitution.

A detailed study of waveguides can also be examined by determining the index of refraction and varying the amount of titanium to change the index of refraction and test the efficiency of the waveguide. A concentration study can be done to determine at what optimal concentrations of rare earth ions can be incorporated into the waveguide to make a compact optical amplifier.

In order to investigate the structure of the Eu^{3+} ions within the sol-gel system. Fluorescence Line Narrowing techniques can be done. Eu^{3+} is a good probe to identifying local structure within glass systems. Moreover, computational techniques such as molecular dynamics and Monte-Carlo can be done to simulate the disordered sol-gel system and further identify the coordination of all atoms in multicomponent systems.